

Bessel Fourier Orientation Reconstruction (BFOR): An analytical diffusion propagator reconstruction for hybrid diffusion imaging and computation of q -space indices

A. Pasha Hosseinbor^{a,b,*}, Moo K. Chung^{b,c}, Yu-Chien Wu^{b,d,e}, Andrew L. Alexander^{a,b,f}

^a Department of Medical Physics, University of Wisconsin-Madison, Madison, WI, USA

^b Waisman Laboratory for Brain Imaging and Behavior, University of Wisconsin-Madison, Madison, WI, USA

^c Department of Biostatistics and Medical Informatics, University of Wisconsin-Madison, Madison, WI, USA

^d Dartmouth Brain Imaging Center, Dartmouth College, Hanover, NH, USA

^e Department of Radiology, University of Wisconsin-Madison, Madison, WI, USA

^f Department of Psychiatry, University of Wisconsin-Madison, Madison, WI, USA

ARTICLE INFO

Article history:

Accepted 21 August 2012

Available online 31 August 2012

Keywords:

Ensemble average propagator

Bi-Gaussian model

Extrapolation

q -Space indices

High angular resolution diffusion imaging

Heat diffusion smoothing

ABSTRACT

The ensemble average propagator (EAP) describes the 3D average diffusion process of water molecules, capturing both its radial and angular contents. The EAP can thus provide richer information about complex tissue microstructure properties than the orientation distribution function (ODF), an angular feature of the EAP. Recently, several analytical EAP reconstruction schemes for multiple q -shell acquisitions have been proposed, such as diffusion propagator imaging (DPI) and spherical polar Fourier imaging (SPFI). In this study, a new analytical EAP reconstruction method is proposed, called Bessel Fourier Orientation Reconstruction (BFOR), whose solution is based on heat equation estimation of the diffusion signal for each shell acquisition, and is validated on both synthetic and real datasets. A significant portion of the paper is dedicated to comparing BFOR, SPFI, and DPI using hybrid, non-Cartesian sampling for multiple b -value acquisitions. Ways to mitigate the effects of Gibbs ringing on EAP reconstruction are also explored. In addition to analytical EAP reconstruction, the aforementioned modeling bases can be used to obtain rotationally invariant q -space indices of potential clinical value, an avenue which has not yet been thoroughly explored. Three such measures are computed: zero-displacement probability (P_0), mean squared displacement (MSD), and generalized fractional anisotropy (GFA).

© 2012 Elsevier Inc. All rights reserved.

Introduction

The aim of diffusion-weighted imaging (DWI) is to non-invasively recover information about the diffusion of water molecules in biological tissues. The most common form of DWI is diffusion tensor imaging (DTI) (Basser et al., 1994), which is a good model of diffusion-weighted signal behavior at low levels of diffusion weighting. However, DTI is limited by the Gaussian assumption, which is invalid at higher levels of diffusion weighting ($b > 2000$ s/mm²) and its inability to resolve multiple fiber orientations within a voxel (Alexander et al., 2001; Frank, 2001; Wiegell et al., 2000). In order to recover complex white matter (WM) geometry, high angular resolution diffusion imaging (HARDI) (Tuch et al., 2002), which reduces the diffusion signal sampling to a single sphere (i.e. single level of diffusion weighting) within q -space, was proposed. Many HARDI techniques (Aganj et al., 2010; Canales-Rodriguez et al., 2009; Descoteaux et al., 2007; Hess et al., 2006; Tuch, 2004) seek to extract the orientation distribution function (ODF), a probability density function describing the angular

distribution of water molecules during diffusion. Unlike apparent diffusion coefficient (ADC) profiles, the maxima of the ODF are aligned with the fiber directions, making it useful in fiber tractography applications. However, the ODF only retrieves the angular content of the diffusion process.

The ensemble average propagator (EAP) provides more information about tissue microstructure than the ODF because it captures both the radial and angular information contained in the diffusion signal. The ODF, mathematically defined as the radial projection of the EAP, is simply an angular feature of the EAP. Unlike the diffusion tensor, the EAP profiles illustrate and recover crossing fibers. The authors in Cohen and Assaf (2002) have suggested that the radial part of the diffusion signal may be sensitive to WM disorders caused by demyelination and could be used to infer the axonal diameter.

The estimation of the EAP requires combination of high angular sampling at multiple levels of diffusion weighting. Under the narrow pulse assumption (Stejskal and Tanner, 1965), the diffusion signal attenuation, $E(\mathbf{q})$ in q -space and the EAP, $P(\mathbf{p})$, are Fourier Transform (FT) pairs (Callaghan, 1991):

$$P(\mathbf{p}) = \int E(\mathbf{q}) e^{-2\pi i \mathbf{q} \cdot \mathbf{p}} d^3 \mathbf{q}. \quad (1)$$

* Corresponding author at: Department of Medical Physics, University of Wisconsin-Madison, Madison, WI, USA.

E-mail address: hosseinbor@wisc.edu (A.P. Hosseinbor).

where $E(\mathbf{q}) = S(\mathbf{q})/S_0$ is the normalized q -space diffusion signal, $S(\mathbf{q})$ is the diffusion signal measured at position \mathbf{q} in q -space, and S_0 is the baseline image acquired without any diffusion gradients ($q=0$). We denote $\mathbf{q} = q \mathbf{u}(\theta, \phi)$ and $\mathbf{p} = p \mathbf{r}(\theta', \phi')$, where \mathbf{u} and \mathbf{r} are 3D unit vectors. The wave vector \mathbf{q} is $\mathbf{q} = \gamma \delta \mathbf{G} / 2\pi$, where γ is the nuclear gyromagnetic ratio and $\mathbf{G} = g\mathbf{u}$ is the applied diffusion gradient direction. The norm of the wave vector, q , is related to the diffusion weighting level (b -value) via $b = 4\pi^2 q^2 (\Delta - \delta/3)$ (Basser, 2002), where δ is the duration of the applied diffusion gradients and Δ the time between the two pulses. Eq. (1) is valid only if the narrow pulse condition is met, which is rarely the case for q -space diffusion MRI performed under experimental conditions. Several studies (Bar-Shir et al., 2008; Mair et al., 2002; Weeden et al., 2005) however, have shown that even when these assumptions do not hold, the Fourier relationship in Eq. (3) is still a reasonable approximation of the microstructural features. The diffusion displacements, however, will be consistently underestimated (Weeden et al., 2005).

Various methods already exist to reconstruct the EAP. Using the diffusion tensor framework, the EAP is simply described by a multivariate Gaussian function (Basser et al., 1994). The authors in Ghosh and Deriche (2010) presented a closed-form approximation of the EAP using higher order tensors, specifically the 4th order diffusion tensor. The diffusion orientation transform (DOT) (Ozarslan et al., 2006) is a HARDI technique that computes the iso-radius of the EAP. DOT assumes the radial diffusion follows a mono-exponential decay, which allows the radial integration in Eq. (1) to be solved analytically. The spherical integration is then solved numerically. The application of this technique, however, is limited by its mono-Gaussian assumption of the radial diffusion decay. In addition, the single shell approach of DOT gives an incomplete picture of the EAP, whose estimation requires signal measurements along all of q -space.

EAP reconstruction techniques using multiple diffusion weighting acquisitions can be divided into two strategies: Fast Fourier Transform (FFT) based and analytical. FFT based methods include diffusion spectrum imaging (DSI) (Canales-Rodriguez et al., 2010; Weeden et al., 2005) and hybrid diffusion imaging (HYDI) (Rathi et al., 2011; Wu and Alexander, 2007). DSI is based on direct sampling of the diffusion signal on a Cartesian q -space lattice. The FT in Eq. (1) is then numerically evaluated via FFT to obtain the EAP. A major advantage of DSI is that the EAP is estimated without any prior assumptions of behavior of the diffusion signal. However, DSI requires dense sampling of the Cartesian lattice, resulting in very long acquisition times. HYDI samples the diffusion signal along concentric spherical shells in q -space, with the measurements then being interpolated and regridded onto a $9 \times 9 \times 9$ Cartesian lattice so that the EAP can be similarly reconstructed as in DSI. HYDI uses much fewer samples than DSI, making it more clinically feasible. However, the HYDI propagator reconstruction may suffer from the *ad hoc* signal interpolation and regridding.

The FFT is impractical for methods employing spherical q -space sampling schemes, such as HYDI, since the FFT requires data to lie on a Cartesian grid. It is also quite computationally expensive. Solving the FT in spherical coordinates (i.e. spherical Fourier Transform) instead, obviates the need for FFT and *ad hoc* processing. Analytical methods, seeking to obtain a closed-form solution of the EAP, pursue such a route. Currently, the two main analytical EAP reconstruction schemes are diffusion propagator imaging (DPI) (Descoteaux et al., 2011) and spherical polar Fourier imaging (SPFI) (Assemlal et al., 2009a; Cheng et al., 2010a, 2010b).

DPI assumes that $E(\mathbf{q})$ is a solution to the 3D Laplace's equation $\nabla^2 E = 0$, which results in the signal basis being composed of the regular and irregular solid harmonics. It is fast, and seems to work well with only a small number of samples. However, the DPI signal basis is an unrealistic model of $E(\mathbf{q})$ because Laplacian modeling of diffusion signal entails that (1) $E(0)$ does not exist, which arises from the irregular solid harmonic term, and (2) MSD of water molecules

is zero, which will be proved in the Theory section. In addition, the DPI signal basis lacks orthonormality, and hence does not possess the robust numerical stability that would otherwise feature in an orthonormal basis.

SPFI models the diffusion signal in terms of an orthonormal basis comprising the spherical harmonics (SH) and Gaussian-Laguerre polynomials. The SPFI signal basis is, in fact, a modified solution of the 3D quantum mechanical simple harmonic oscillator problem. It is robust to noise and low anisotropy, and works well with just a few number of samples. However, SPFI has not been tested at $b > 3000$ s/mm². A slightly modified version of the SPFI signal basis was proposed just recently by the authors in Caruyer and Deriche (2012). This paper, however, will only be concerned with the original SPFI basis.

A closely related basis to SPFI was proposed in Ozarslan et al. (2008, 2009), which use the Hermite polynomials to estimate the 1D q -space diffusion signal. In addition to forming a complete orthogonal basis, the Hermite polynomials are also eigenfunctions of the Fourier transform. However, the 3D EAP solution has yet to be derived using this basis.

With respect to analytical EAP reconstruction methods, one valuable though overlooked use is in extracting rotationally invariant quantitative measures from them. Recently, the authors in Assemlal et al. (2011) used the SPFI signal basis to compute the novel fiber population dispersion (FPD), an index which assess the presence of crossing fibers within a voxel. The FPD, however, is a relatively new measure that has not yet been computed for an actual human brain. More well-established q -space metrics include generalized fractional anisotropy (GFA) (Tuch, 2004), mean squared displacement (MSD) (Assaf et al., 2000; Wu and Alexander, 2007), and zero-displacement probability (P_0) (Assaf et al., 2000). All three are simply scalar features of the EAP, and the GFA and the MSD can be viewed as high angular resolution analogues of the DTI indices fractional anisotropy (FA) and mean diffusivity (MD) (Basser and Pierpaoli, 1996), respectively. An analytical representation of the EAP (and hence diffusion signal) can facilitate either analytic computation of such features or numerical efficiency in estimating them.

In this paper, we present Bessel Fourier Orientation Reconstruction (BFOR) (Hosseinbor et al., 2011). Rather than assuming the signal satisfies Laplace's equation, we reformulate the problem into a Cauchy problem and assume $E(\mathbf{q})$ satisfies the heat equation. The heat equation is a generalization of Laplace's equation, which the latter approaches at the steady state (i.e. $t \rightarrow \infty$). BFOR provides an analytical reconstruction of the EAP profile from diffusion signal and models the diffusion signal in terms of an orthonormal basis. In addition, it contains an intrinsic exponential smoothing term that allows one to control the amount of smoothing in the EAP estimation. The last point is significant because, although the Laplacian modeling intrinsically smooths the diffusion signal, the amount of smoothing cannot be controlled, and hence it may oversmooth the signal. In addition to heat diffusion smoothing, we also look at linear signal extrapolation as a potential means to mitigate the effects of common artifacts afflicting the reconstructed EAP profile, such as Gibbs ringing and signal truncation. Employing a hybrid, non-Cartesian encoding scheme in both synthetic and *in vivo* datasets, we reconstruct the EAP using BFOR, SPFI, and DPI and assess their performances. Lastly, we use BFOR to compute GFA, P_0 , and MSD, and compare BFOR's accuracy in estimating such indices to that of DPI and SPFI.

The paper is organized as follows: in Theory section, we develop BFOR, first by describing how to estimate the diffusion signal, and then deriving the analytical solution for the EAP using Eq. (1). Scalar features of the EAP are also introduced in this section. The Appendix carefully details the derivations of the BFOR signal basis, EAP, and q -space indices. In Materials and methods section, we describe the implementation details of BFOR and present the synthetic and *in vivo* human brain datasets that will be used to validate and

illustrate BFOR and compare it to SPFI and DPI in [Results](#) section. Lastly, we discuss our results and future applications of analytical EAP methods in [Discussion](#) section.

Theory

The heat equation is ubiquitous in the natural sciences, arising in Fick's law of diffusion, Brownian motion, Fourier's law of thermal conduction, and the price variation over time of stocks. A nice feature of any solution to the heat equation is its temporal dependence, which can be viewed as an inherent smoothing control mechanism. DPI, by solving the heat equation at the steady state, has no smoothing control mechanism, and so can potentially oversmooth the signal. Smoothing can be useful in situations where reconstructions greatly suffer from noise. Although our method is similar in spirit to DPI and SPFI, it significantly differs from them due to its inclusion of a smoothing term.

Consider the eigenvalue/boundary condition problem

$$\nabla_{\mathbf{q}} \psi_i(\mathbf{q}) = -\lambda_i \psi_i(\mathbf{q}), \quad \psi_i(q = \tau, \mathbf{u}) = 0 \tag{2}$$

which we use to solve the Cauchy problem

$$\frac{\partial}{\partial t} g(\mathbf{q}, t) - \nabla_{\mathbf{q}} g(\mathbf{q}, t) = 0, \quad g(\mathbf{q}, t = 0) = f(\mathbf{q}), \tag{3}$$

where $f(\mathbf{q})$ is simply the acquired signal and ∇ is some self-adjoint linear operator. We require $\lambda > 0$. [Chung et al. \(2007\)](#) derived a unique solution for Eq. (3):

$$g(\mathbf{q}, t) = \sum_{i=0}^{\infty} a_i e^{-\lambda_i t} \psi_i(\mathbf{q}), \tag{4}$$

where $e^{-\lambda_i t}$ is a smoothing term controlled by parameter $t \geq 0$ and the coefficients are given by $a_i = \langle f, \psi_i \rangle$. The implication of Eq. (4) is that the solution decreases exponentially as t increases and smoothes out high spatial frequency noise much faster than low-frequency noise. In DPI, however, the steady state assumption permanently removes any temporal term, which governs the extent of smoothing, so there is no smoothing control mechanism. Note that $t=0$ corresponds to no smoothing being applied.

Assuming that $\nabla = \nabla^2$, where ∇^2 is the 3D Laplacian operator in spherical coordinates, Eq. (2) becomes

$$\left[\frac{1}{q^2} \frac{\partial}{\partial q} \left(q^2 \frac{\partial}{\partial q} \right) + \frac{1}{q^2 \sin \theta} \frac{\partial}{\partial \theta} \left(\sin \theta \frac{\partial}{\partial \theta} \right) + \frac{1}{q^2 \sin^2 \theta} \frac{\partial^2}{\partial \phi^2} \right] \psi_i(\mathbf{q}) = -\lambda_i \psi_i(\mathbf{q}) \tag{5}$$

Eq. (5) can be solved via separation of variables to obtain an orthonormal basis, which we show in [Appendix A](#):

$$\psi_{nj}(\mathbf{q}) = j_{l(j)} \left(\frac{\alpha_{nl(j)} q}{\tau} \right) Y_j(\mathbf{u}), \tag{6}$$

where $\alpha_{nl(j)}$ is n th root of l th order spherical Bessel function of first kind j_l and τ is the radial distance in q -space at which the Bessel function goes to zero. Y_j are a modified real and symmetric SH basis proposed in [Descoteaux et al. \(2011\)](#) to reflect the symmetry and realness of the diffusion signal. The index $j := j(l, m) = (l^2 + l + 2) / 2 + m$ is defined for $l = 0, 2, 4, \dots$ and $m = -l, \dots, 0, \dots, l$. Hence, for $j = \{1, 2, 3, 4, 5, 6, 7, \dots\}$, $l(j) = \{0, 2, 2, 2, 2, 2, 4, \dots\}$. The eigenvalues are $-\lambda_{nl(j)} = -\frac{\alpha_{nl(j)}^2}{\tau^2}$. The SH are also used to model the angular profile of the diffusion signal in DPI and SPFI.

Within the context of our problem, $g(\mathbf{q}, t)$ is the diffusion signal. The assumption of a Laplacian operator results in Eq. (3) becoming the heat equation: $\nabla^2 E(\mathbf{q}, t) = \frac{\partial E(\mathbf{q}, t)}{\partial t}$. From Eq. (4) then, the diffusion

signal can be expanded in terms of the spherical orthonormal basis ψ_{nj} given in Eq. (6):

$$E(\mathbf{q}, t) = \sum_{n=1}^N \sum_{j=1}^R C_{nj} e^{-\frac{\alpha_{nl(j)}^2 t}{\tau^2}} j_{l(j)} \left(\frac{\alpha_{nl(j)} q}{\tau} \right) Y_j(\mathbf{u}), \tag{7}$$

where C_{nj} are the expansion coefficients, $R = \frac{(L+1)(L+2)}{2}$ is the number of terms in the modified SH basis of truncation order L , and N is the number of roots for any spherical Bessel function of order l . The total number of coefficients in the expansion is $W = \frac{N(L+1)(L+2)}{2}$. Note that the actual acquired signal from scanner is given at $t=0$. In DWI, $E(0) = 1$, and so for our basis, we obtain the following identity (derived in [Appendix B](#)):

$$E(q = 0, \mathbf{u}, t = 0) = \frac{1}{\sqrt{4\pi}} \sum_n C_{n1} = 1, \tag{8}$$

which holds for any \mathbf{u} within the unit sphere S^2 (i.e. $\mathbf{u} \in S^2$).

An important property of the diffusion signal is that it asymptotically approaches zero as $q \rightarrow \infty$. However, the spherical Bessel functions infinitely oscillate about zero, as shown in [Fig. 1](#), so a finite upper bound τ is needed at which the BFOR signal model becomes zero. The fact that the radial basis in BFOR does not radially decay to zero but becomes zero at some point in q -space is the main limitation of the BFOR algorithm.

In deriving the EAP, the spherical integration of Eq. (1) is made easier by expressing the Fourier kernel as a plane wave expansion:

$$e^{-2\pi i \mathbf{q} \cdot \mathbf{p}} = 4\pi \sum_{j=1}^{\infty} (-i)^{l(j)} j_{l(j)}(2\pi q p) Y_j(\mathbf{u}) Y_j(\mathbf{r}) \tag{9}$$

Substituting Eqs. (7) and (9) into Eq. (1), we obtain

$$\begin{aligned} P(\mathbf{p}, t) &= 4\pi \int \sum_{n=1}^N \sum_{j=1}^R C_{nj} e^{-\frac{\alpha_{nl(j)}^2 t}{\tau^2}} j_{l(j)} \left(\frac{\alpha_{nl(j)} q}{\tau} \right) Y_j(\mathbf{u}) \\ &\quad \times \sum_{j=1}^{\infty} (-i)^{l(j)} j_{l(j)}(2\pi q p) Y_j(\mathbf{u}) Y_j(\mathbf{r}) d^3 \mathbf{q} \\ &= 4\pi \sum_{n=1}^N \sum_{j=1}^R (-1)^{l(j)/2} C_{nj} e^{-\frac{\alpha_{nl(j)}^2 t}{\tau^2}} Y_j(\mathbf{r}) I_{nl(j)}(p), \end{aligned} \tag{10}$$

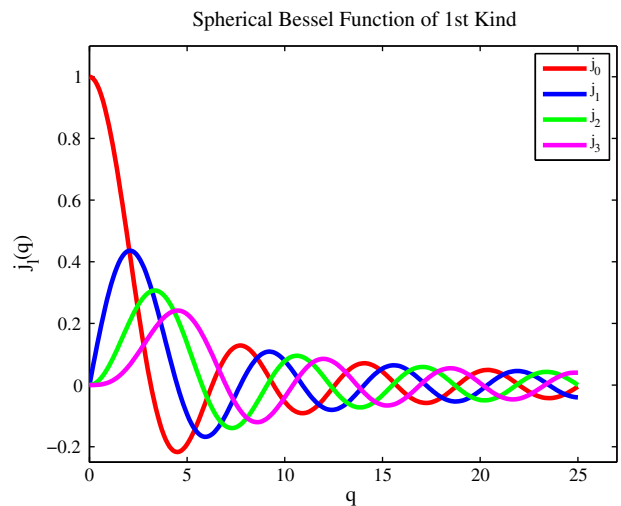


Fig. 1. Plots of spherical Bessel functions of first kind, which form the radial basis of the BFOR signal solution, for different orders l . As q approaches infinity, they infinitely oscillate about zero.

where we use the orthonormal property of SH, i.e. $\int Y_j(\mathbf{u})Y_j(\mathbf{u})d^2\mathbf{u} = \delta_{jj}$ and define

$$I_{nl(j)}(p) = \int_0^\infty q^2 J_{l(j)}\left(\frac{\alpha_{nl(j)}q}{\tau}\right) J_{l(j)}(2\pi qp) dq \approx \int_0^\tau q^2 J_{l(j)}\left(\frac{\alpha_{nl(j)}q}{\tau}\right) J_{l(j)}(2\pi qp) dq \quad (11)$$

The integral in Eq. (11) is solved in Appendix C, and we can write the EAP as

$$P(\mathbf{p}, t) = 2\tau \sqrt{2\pi^3} \sum_{n=1}^N \sum_{j=1}^R (-1)^{\frac{nl}{2}} C_{nj} e^{-\frac{q_{nl}^2 t}{2\tau^2}} Y_j(\mathbf{r}) \frac{\sqrt{\alpha_{nl(j)} J_{l(j)-1/2}\left(\frac{\alpha_{nl(j)} q}{\tau}\right) J_{l(j)}(2\pi\tau p)}{\left(4\pi^2 p^2 - \frac{\alpha_{nl}^2}{\tau^2}\right)} \quad (12)$$

The BFOR theoretical solution can be summarized in five steps:

1. $\nabla^2 \psi_i(\mathbf{q}) = -\lambda_i \psi_i(\mathbf{q}), \psi_i(q = \tau, \mathbf{u}) = 0$
2. $E(\mathbf{q}, t) = \sum_{i=0}^\infty a_i h_i(t) \psi_i(\mathbf{q})$
3. $\nabla^2 E(\mathbf{q}, t) = \frac{\partial E(\mathbf{q}, t)}{\partial t}, E(\mathbf{q}, t = 0) = f(\mathbf{q})$
4. $h_i(t) = e^{-\lambda_i t}; a_i = \langle f(\mathbf{q}), \psi_i(\mathbf{q}) \rangle$
5. $P(\mathbf{p}, t) = \int E(\mathbf{q}, t) e^{-2\pi i \mathbf{q} \cdot \mathbf{p}} d^3 \mathbf{q} = 4\pi \sum_{j=1}^\infty (-i)^{l(j)} Y_j(\mathbf{r}) \left\{ \int E(\mathbf{q}, \mathbf{u}, t) j_{l(j)}(2\pi qp) Y_j(\mathbf{u}) d^3 \mathbf{q} \right\}$

Rotationally invariant q -space indices

In addition to analytical EAP reconstruction, the DPI, BFOR, and SPFI modeling bases can be used to obtain rotationally invariant q -space indices. Here, we look at three such measures: P_0 , MSD, and GFA.

$P_0 = P(\mathbf{p} = 0)$ is the probability density that a water molecule returns back to its initial position within the diffusion time [6,50]. In a healthy adult brain, P_0 is greater in white matter (WM) than gray matter (GM) because WM has more restricting barriers including multi-layer myelin sheaths, axonal membranes, and microtubules. Such restrictivity increases the likelihood of a water molecule returning to its original position, whereas it has a very low probability of returning to its original position in areas of unrestricted isotropic diffusion (CSF). Hence, P_0 can be viewed as a measure of restricted diffusion. Several studies have shown P_0 to be sensitive to brain pathology, and suggesting that changes in myelin are the primary mechanism for differences in P_0 (Assaf et al., 2002; Bar-Shir et al., 2009; Wu et al., 2011).

P_0 can be evaluated either numerically or analytically. The authors in Wu et al. (2008) computed P_0 by numerically summing the normalized diffusion signal $E(\mathbf{q})$ over all diffusion measurements in q -space, and then correcting the sum by the sampling density. Analytical formulations of P_0 were derived for the SPFI and DPI signal bases

Materials and methods

In general, we are given k HARDI shell datasets. The number of encoding directions in each shell does not have to be the same. Each HARDI dataset corresponds to a different b -value. Across all k shells, we have a total of M diffusion measurements (including the $b = 0$ measurement). Hence, from these multiple shell datasets, we want to reconstruct the EAP, $P(\mathbf{p})$.

Numerical implementation of BFOR

The task is to estimate coefficients C_{nj} in Eq. (12) from the observed signal $E(q, \mathbf{u}, t = 0)$. We achieve this by carrying out a linear least square (LLS) fitting with regularization in the radial and angular parts. We let $\mathbf{S} = [E(\mathbf{q}_1, t = 0) \dots E(\mathbf{q}_M, t = 0)]^T$ be the $M \times 1$ vector representing the M diffusion signal measurements across all k shells. We also let \mathbf{C} represent the $W \times 1$ vector of unknown expansion coefficients C_{nj} , where $W = \frac{N(L+1)(L+2)}{2}$. Defining $Z_{nj}(q, \mathbf{u}) = j_{l(j)}(\alpha_{nl(j)}q/\tau) Y_j(\mathbf{u})$, we let \mathbf{Z} denote our $M \times W$ design matrix:

$$\mathbf{Z} = \begin{pmatrix} Z_{1,1}(q_1, \mathbf{u}_1) & Z_{2,1}(q_1, \mathbf{u}_1) & \dots & Z_{N,1}(q_1, \mathbf{u}_1) & \dots & Z_{1,R}(q_1, \mathbf{u}_1) & Z_{2,R}(q_1, \mathbf{u}_1) & \dots & Z_{N,R}(q_1, \mathbf{u}_1) \\ \vdots & \vdots & \ddots & \vdots & \ddots & \vdots & \vdots & \ddots & \vdots \\ Z_{1,1}(q_M, \mathbf{u}_M) & Z_{2,1}(q_M, \mathbf{u}_M) & \dots & Z_{N,1}(q_M, \mathbf{u}_M) & \dots & Z_{1,R}(q_M, \mathbf{u}_M) & Z_{2,R}(q_M, \mathbf{u}_M) & \dots & Z_{N,R}(q_M, \mathbf{u}_M) \end{pmatrix}$$

(Cheng et al., 2010b; Descoteaux et al., 2011). Similarly, an analytical P_0 expression can be obtained using the BFOR basis, which is derived in Appendix D:

$$P_{0\text{BFOR}} = 2\sqrt{\pi}\tau^3 \sum_{n=1}^N C_{n1} \frac{(-1)^{n+1}}{\alpha_{n0}^2} \quad (13)$$

The MSD, which we will denote as $\langle p^2 \rangle$, is simply the second moment of the EAP (Wu and Alexander, 2007): $\langle p^2 \rangle = \int p^2 P(\mathbf{p}) d^3 \mathbf{p}$. It is related to the MD, which in the case of Gaussian diffusion is given by the well-known Einstein relation $\langle p^2 \rangle = 6(\Delta - \delta/3)MD$. Thus far, an analytical formulation of MSD exists only within the DTI framework. It is calculated numerically in q -space imaging, either by extracting the full width at half maximum of the EAP (Assaf et al., 2000) or taking the geometric mean of the diffusion signal over all directions on a HDYI shell (Wu et al., 2008) In Appendix E, we will show that, in general, the MSD is related to the diffusion signal by the relation

$$\langle p^2 \rangle = \frac{-1}{4\pi^2} \nabla^2 E(\mathbf{q}) \Big|_{\mathbf{q}=0} \quad (14)$$

Since DPI assumes $\nabla^2 E = 0$, it predicts the MSD to be zero: $\langle p^2 \rangle_{\text{DPI}} = 0$. The BFOR MSD is (derived in Appendix E)

$$\langle p^2 \rangle_{\text{BFOR}} = \frac{1}{8\pi^2 \tau^2} \sum_{n=1}^N C_{n1} \alpha_{n0}^2 \quad (15)$$

Tuch (2004) introduced the concept of GFA and defined it as $\text{std}(\text{ODF})/\text{rms}(\text{ODF})$. Since ODF is only a feature of the EAP, the subsequent GFA map is derived solely from the angular content of the diffusion profile. Incorporating both the angular and radial contents of the diffusion profile into the definition of GFA will result in a radial dial of GFA maps, illustrating how anisotropy varies with diffusion displacement p . Therefore, we define a new GFA:

$$GFA(p = p_0) = \frac{\text{std}[P(p = p_0, \mathbf{r})]}{\text{rms}[P(p = p_0, \mathbf{r})]} \quad (16)$$

Another advantage of Eq. (16) is that it is better suited for multiple diffusion weighted MR experiments, unlike Tuch's definition, which is single-shell HARDI-based. In order to capture the 3D anisotropy of the EAP-defined GFA maps, 1000 uniformly distributed vertices on a unit sphere in propagator space (i.e. 1000 values of θ' and ϕ') were acquired using the approach described in Wong and Roos (1994).

Table 1
HYDI encoding scheme for synthetic and human datasets.

Shell	Ne	q (mm ⁻¹)	Δq (mm ⁻¹)	b (s/mm ²)
	1	0		0
1st	6	15.2	15.2	375
2nd	21	30.4	15.2	1500
3rd	24	45.6	15.2	3375
4th	24	60.8	15.2	6000
5th	50	76	15.2	9375
	Total = 126	$q_{max} = 76$	Mean = 15.2	$b_{max} = 9375$

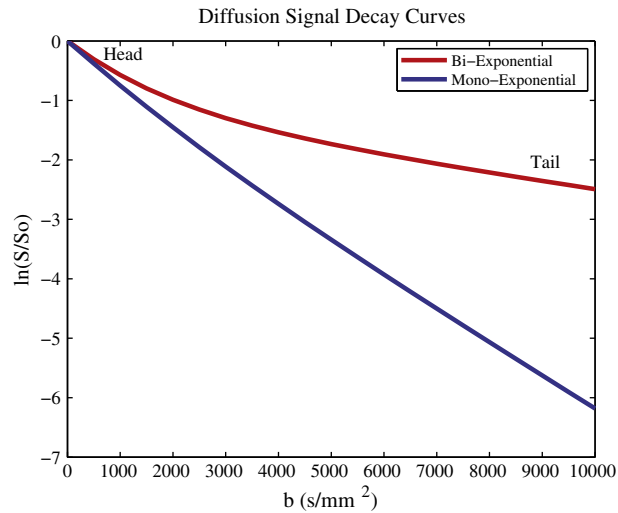


Fig. 2. Plots of diffusion signal attenuation as a function of b -value illustrating mono-exponential and bi-exponential decays. The tail of the bi-exponential can be interpreted as the slow diffusion component, while the head the fast diffusion component.

Thus, we have a simple linear model of the form $\mathbf{S} = \mathbf{Z}\mathbf{C}$. This system of over-determined equations is solved with a regularized LLS solution yielding vector $\hat{\mathbf{C}}$ given by

$$\hat{\mathbf{C}} = \left(\mathbf{Z}^T \mathbf{Z} + \lambda_l \mathbf{L}_{reg} + \lambda_r \mathbf{N}_{reg} \right)^{-1} \mathbf{Z}^T \mathbf{S}, \quad (17)$$

where \mathbf{L}_{reg} is the Laplace–Beltrami regularization diagonal matrix with $l^2(l+1)^2$ entries on the diagonal and \mathbf{N}_{reg} is the regularization diagonal matrix for the radial basis, with entries $n^2(n+1)^2$ on the diagonal. The angular and radial regularization matrices penalize, respectively, high degrees of the angular and radial parts of Eq. (7) in the estimation under the assumption that they are likely to capture noise (Assemlal et al., 2009a). They also serve to reinforce the positivity constraint of the EAP. λ_l and λ_r are the regularization terms for angular and radial bases, respectively.

Visualization of EAP

Lastly, from the estimated vector $\hat{\mathbf{C}}$, we can extract the C_{ij} coefficients needed to compute the EAP, P_0 , MSD, and GFA. The spherical function $P(p, \mathbf{r}, t)$ is the iso-probability profile at some instant of smoothening t for a given p —that is, the probability density that a water molecule, initially at the origin, diffuses a distance p along the direction \mathbf{r} . It is computed by generating 800 equidistant points along the equator of a sphere of radius p i.e. the polar angle θ is fixed at $\pi/2$ and the azimuthal angle ϕ is uniformly varied from 0 to 2π . The EAP profile $P(p, \mathbf{r}, t)$ is then interpolated along these 800 points. Thus, the resulting profiles are 2D with the equator perpendicular to the z -axis. It is important to note that in this paper smoothening was applied only to the EAP, itself, and not on the diffusion signal.

Value of τ parameter

An important point to consider in the implementation is how to determine the parameter τ in the signal basis. In practice, the diffusion signal is bounded by the maximal q -value q_{max} achievable by the imaging system. The authors in Assaf and Cohen (1998) have shown that, depending

Table 2
Fast/Slow diffusion ADCs and component size fractions (from Maier et al., 2004).

Region of interest	Corpus callosum	Internal capsule
ADC_f ($\mu\text{m}^2/\text{ms}$)	1.176	1.201
ADC_s ($\mu\text{m}^2/\text{ms}$)	0.195	0.176
f_f	0.699	0.643
f_s	0.301	0.357

on the length of diffusion time, the amount of signal present at b -values near $30,000 \text{ s/mm}^2$ varies from about half a percent to about 5%, which means that the signal does not approach zero at q_{max} unless the diffusion weighting/diffusion time are very high/long. Thus, we conclude $\tau \geq q_{max}$. Based on numerical simulations, we find the value of τ that best reconstructs the EAP to be $\tau_{optimal} = q_{max} + \Delta q$, where Δq is the (uniform) q -space sampling interval.

Diffusion MRI data acquisitions for synthetic and human brain data

The synthetic and *in vivo* datasets use a hybrid, non-Cartesian sampling scheme (Wu and Alexander, 2007), shown in Table 1. Since EAP reconstruction is sensitive to angular resolution, the number of encoding directions is increased with each shell to increase the angular resolution with the level of diffusion weighting. The number of directions in the outer shells was increased to better characterize complex tissue organization. Diffusion tensor elements for measurements in the second shell were calculated using non-linear least squares estimation with the Camino software package (Cook et al., 2006), which were then used to obtain the FA and principal eigenvector.

Synthetic data

The mono-exponential (also referred to as mono-Gaussian) mixture model (Tuch et al., 2002) is frequently used to generate synthetic data to validate a given EAP reconstruction, such as in Assemlal et al. (2009a), Cheng et al. (2010b), where the maximum b -value used was 3000 s/mm^2 . However, diffusion MR imaging experiments using high b -values ($>2000 \text{ s/mm}^2$) have shown that the diffusion signal decay is no longer mono-exponential. Studies in normal human brain, with b -values over an extended range of up to 6000 s/mm^2 , have shown that the signal decay is better described with a bi-exponential i.e. bi-Gaussian curve (Clark and Le Bihan, 2000; Mulkern et al., 1999). Similar findings were made for rat brain, using multiple b -values of up to $10,000 \text{ s/mm}^2$ (Niendorf et al., 1996). According to Assaf and Cohen (1998), a bi-exponential fit gives very good agreement with the observed water signal attenuation in excised brain tissue from rats for b -values of up to $2 - 3 \times 10^4 \text{ s/mm}^2$. Thus, BFOR, SPFI, and DPI were applied to simulations of crossing fiber configurations generated by a bi-Gaussian mixture model. Fig. 2 illustrates mono-exponential and bi-exponential decay curves, where the latter has a pronounced tail at high q values, indicating that it takes longer for the signal to decay to zero than under the mono-exponential assumption. The head and tail of the bi-exponential decay curve can be viewed as the fast and slow diffusion components, respectively (Clark and Le Bihan, 2000; Maier et al., 2004).

In bi-Gaussian mixture,

$$E(q, \mathbf{u}) = \sum_{k=1}^{N_b} [f_{kf} e^{-b\mathbf{u}^T \mathbf{D}_{kf} \mathbf{u}} + f_{ks} e^{-b\mathbf{u}^T \mathbf{D}_{ks} \mathbf{u}}], \quad (18)$$

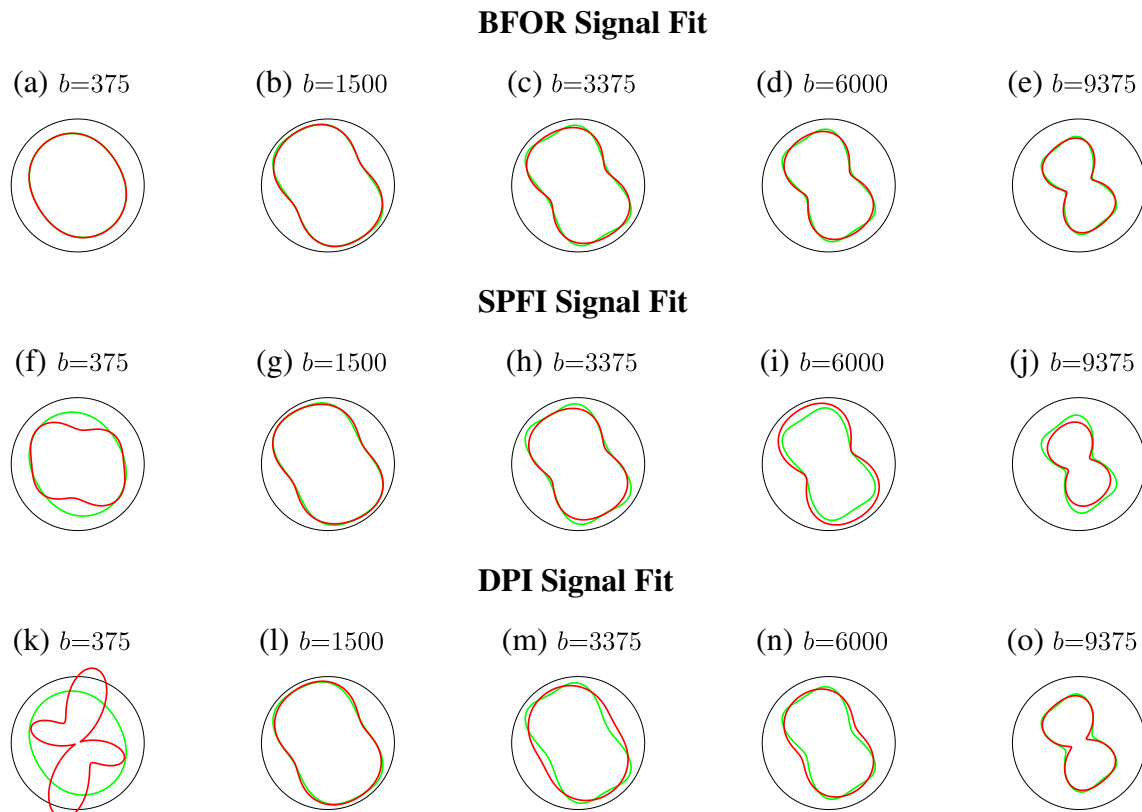


Fig. 3. The ground truth diffusion signal (green) and estimated signal (red) using BFOR, SPFI, and DPI when noise was absent. Two equally weighted WM fibers were simulated crossing at 60° . Measurements from all 5 shells were used.

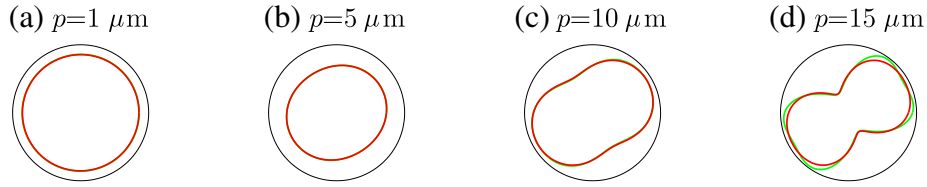
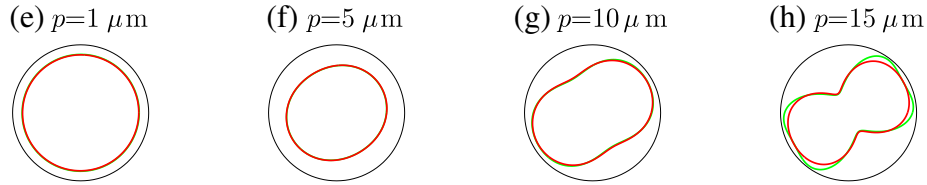
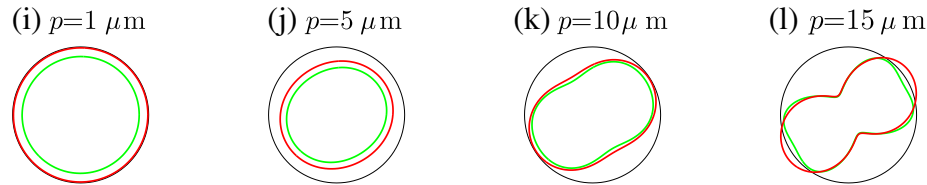
BFOR Fast EAP reconstruction at $t = 0$ **SPFI Fast EAP Reconstruction****DPI Fast EAP Reconstruction**

Fig. 4. Reconstruction of the fast component EAP (red) using BFOR, SPFI, and DPI compared with the ground truth (green). Two equally weighted WM fibers were simulated crossing at 60° .

where N_b is the total number of simulated fibers, f_{kf} the volume fraction of the fast component of the k^{th} fiber, and f_{ks} the volume fraction of the slow component. The summation of all volume fractions is 1, i.e., $\sum_{k=1}^{N_b} [f_{kf} + f_{ks}] = 1$. D_{kf} and D_{ks} describe the diffusion tensor for the fast and slow components, respectively, of the k^{th} fiber assuming no exchange between the fast- and slow-diffusion compartments. It should be noted

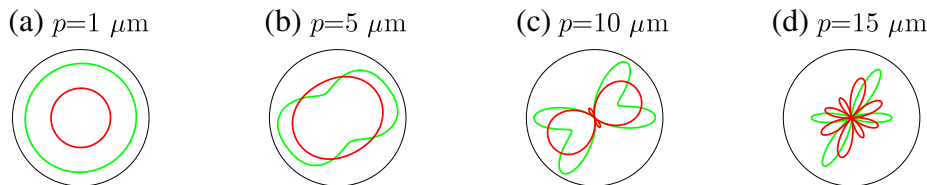
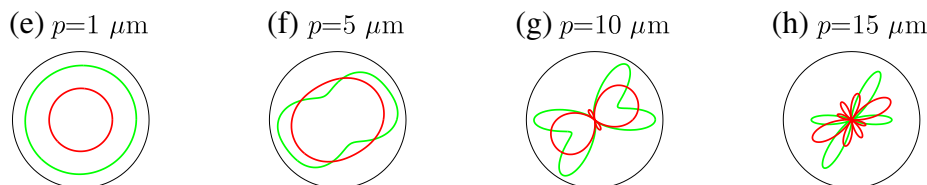
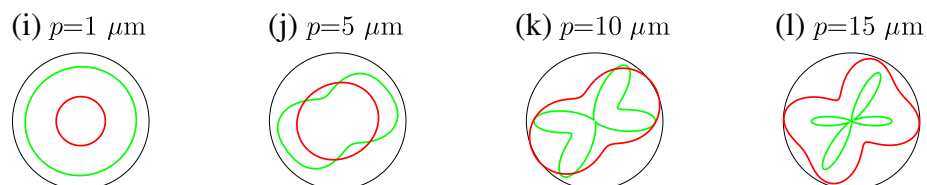
BFOR Slow EAP Reconstruction at $t = 0$ **SPFI Slow EAP Reconstruction****DPI Slow EAP Reconstruction**

Fig. 5. Reconstruction of the slow component EAP (red) using BFOR, SPFI, and DPI compared with the ground truth (green). Two equally weighted WM fibers were simulated crossing at 60° .

that there is controversy over the assignment of these components and whether the bi-Gaussian model should take into account exchange between compartments (Mulkern et al., 1999). The ground truth of EAP is then

$$P(p, \mathbf{r}) = \sum_{k=1}^{N_b} \left[\frac{f_{kf}}{\sqrt{(4\pi\epsilon)^3 |\mathbf{D}_{kf}|}} e^{-p^2 \mathbf{r}^T \mathbf{D}_{kf}^{-1} \mathbf{r}/4\epsilon} + \frac{f_{ks}}{\sqrt{(4\pi\epsilon)^3 |\mathbf{ctD}_{ks}|}} e^{-p^2 \mathbf{r}^T \mathbf{D}_{ks}^{-1} \mathbf{r}/4\epsilon} \right], \quad (19)$$

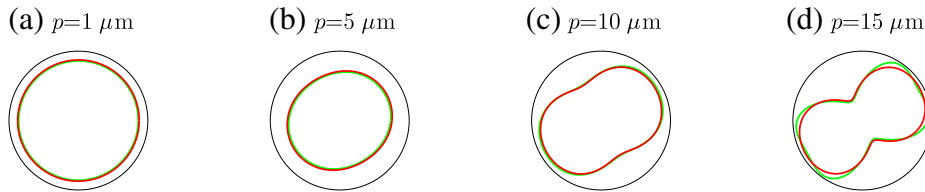
where $\epsilon = \Delta - \delta/3$. For the synthetic data, the diffusion gradient duration is $\delta = 45$ ms and diffusion gradient separation $\Delta = 56$ ms.

In reconstructing the EAP, we look at two equally weighed fibers crossing at 60° , and set eigenvalues of each diffusion tensor to be $[1.6, 0.4, 0.4]e^{-3}$, which gives an FA value of 0.7071. The values of the fast and slow Gaussian diffusion functions were taken from Maier et al. (2004) and are shown in Table 2. Monte Carlo noise simulations were then performed to investigate the effect of SNR on the estimation of P_0 , MSD, and GFA for a single voxel for each EAP method. Seven SNR levels ($[10 \ 20 \ 30 \ 40 \ 50 \ 60 \ 100]$) for the $b=0$ image were simulated, 1000 times each, by adding Rician noise in a similar manner as in Descoteaux et al. (2007) for four different scenarios: a fast isotropic component ($D = 0.00115 \text{ mm}^2/\text{s}$); a slow isotropic component ($D = 0.00045 \text{ mm}^2/\text{s}$); fast anisotropic components of a corpus callosum fiber and internal capsule fiber crossing at 60° ; and the slow anisotropic components for the previous scenario. The BFOR parameters are $\{L=4, N=6, \tau=91.2 \text{ mm}^{-1}, \lambda_l=10^{-6}, \lambda_n=10^{-6}\}$, DPI parameters $\{L=4, \lambda_l=0 \text{ (no noise)}/\lambda_l=0.006 \text{ (with noise)}\}$, and SPFI parameters $\{L=4, N=3, \zeta=500, \lambda_l=10^{-8}, \lambda_n=10^{-8}\}$. For each method, model parameters were chosen based on giving the optimal EAP reconstruction when no noise was present.

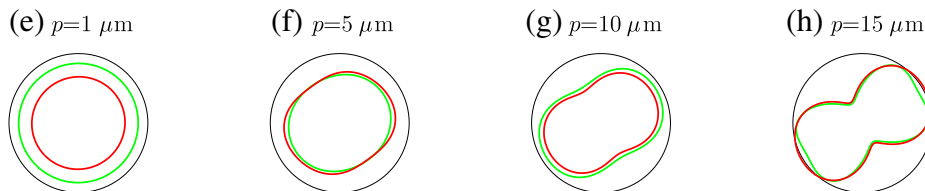
Human brain data

HYDI was performed on a healthy, adult human using a 3.0T GE-SIGNA scanner with an 8-channel head coil and ASSET parallel imaging. The DW pulse sequence was a single-shot, spin-echo, echo-planar imaging (SS-SE-EPI) with pulse-oximeter gating. The MR parameters were as

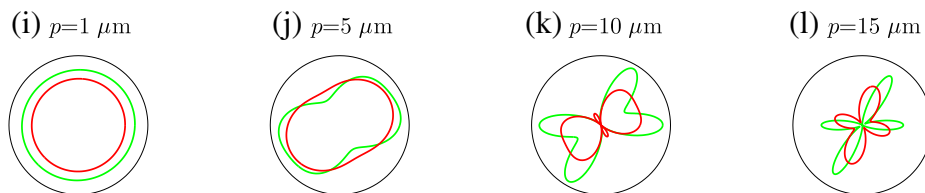
BFOR Fast EAP Reconstruction at $t = 0$ with Linear Extrapolation



SPFI Fast EAP Reconstruction with Linear Extrapolation



BFOR Slow EAP Reconstruction at $t = 0$ with Linear Extrapolation



SPFI Slow EAP Reconstruction with Linear Extrapolation

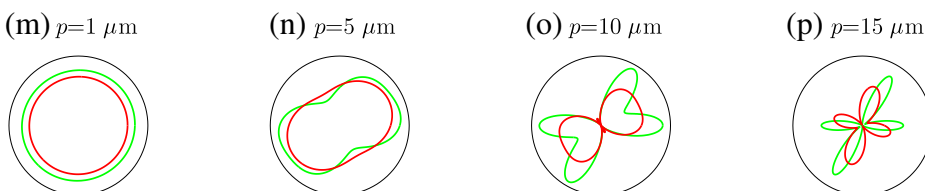


Fig. 6. Extrapolated samples were acquired by linearly damping the signal measurements in the outermost shell. Reconstruction of the EAP (red) using BFOR and SPFI compared with the ground truth (green). Two equally weighted WM fibers were simulated crossing at 60° .

follows: TE = 122 ms, TR 12 s, FOV = 256 mm, matrix = 128×128 , voxel size = $2 \times 2 \text{ mm}^2$, 30 slices with slice thickness = 3 mm, and a total scan time of about 30 min. Diffusion parameters were maximum b -value $b_{max} = 9375 \text{ s/mm}^2$, diffusion gradient duration $\delta = 45 \text{ ms}$, diffusion gradient separation $\Delta = 56 \text{ ms}$, q -space sampling interval $\Delta q = 15.2 \text{ mm}^{-1}$, maximum length of the q -space wave vector $q_{max} = 76 \text{ mm}^{-1}$, field of view of the diffusion displacement space $FOV_p = (1/\Delta q) = 65 \mu\text{m}$, and resolution of the diffusion displacement space $\Delta p = (1/2q_{max}) = 6.6 \mu\text{m}$ (Callaghan, 1991). The same BFOR, DPI, and SPFI modeling parameters utilized for synthetic data were also used for *in vivo* data.

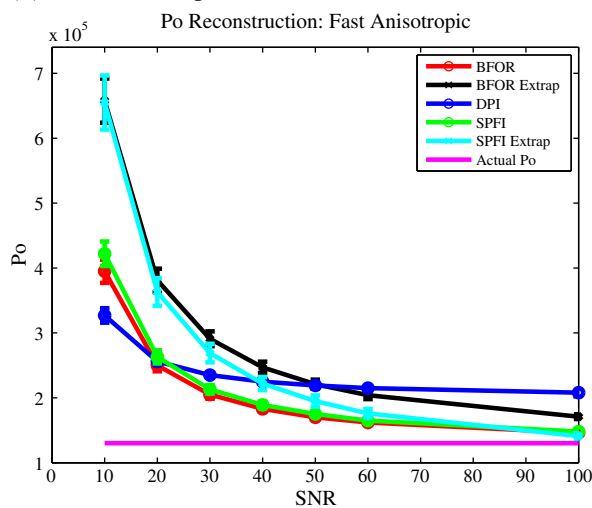
Results

BFOR, DPI, and SPFI are first applied to the numerical phantom and then on the real dataset. The numerical phantom is used to validate BFOR, compare its performance to those of DPI and SPFI, assess all three methods' robustness in estimating the scalar measures P_o , MSD, and GFA, and answer the following questions: (1) Can these methods properly reconstruct a diffusion signal acquired via hybrid sampling? (2) How does the slow diffusion component affect the EAP reconstruction and the estimations of the scalar quantities? (3) What can be done to reduce the effects of Gibbs ringing on the EAP reconstructions? It is also important to note that the EAP and quantitative scalar measures were reconstructed using only 125 diffusion measurements, while those presented in Descoteaux et al. (2011) used 256.

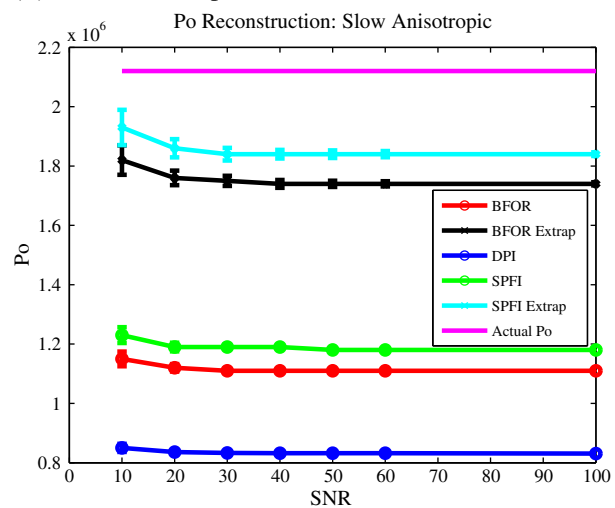
Results of synthetic data

Can these methods be used for diffusion signal estimation? Fig. 3 displays the BFOR, DPI, and SPFI signal fit for each shell and the corresponding ground truth. The BFOR signal basis fits the diffusion signal nearly perfectly for all shells. Both SPFI and DPI reasonably fit the diffusion signal for $b \geq 1500 \text{ s/mm}^2$, but poorly reconstruct the inner most shell ($b = 375 \text{ s/mm}^2$). As expected, DPI also tends to oversmooth the diffusion signal, especially so at $b = 3375, 6000 \text{ s/mm}^2$. Results of DPI signal fitting were also reported in Descoteaux et al. (2011), where uniform sampling along four spherical shells ($b = 2000, 4000, 6000, \text{ and } 8000 \text{ s/mm}^2$) was done. Although a hybrid sampling scheme is used here, our results are consistent with those of Descoteaux et al. (2011) for $b \geq 1500 \text{ s/mm}^2$. SPFI's and DPI's poor signal fit of the diffusion signal in inner most shell may be due to the fact that

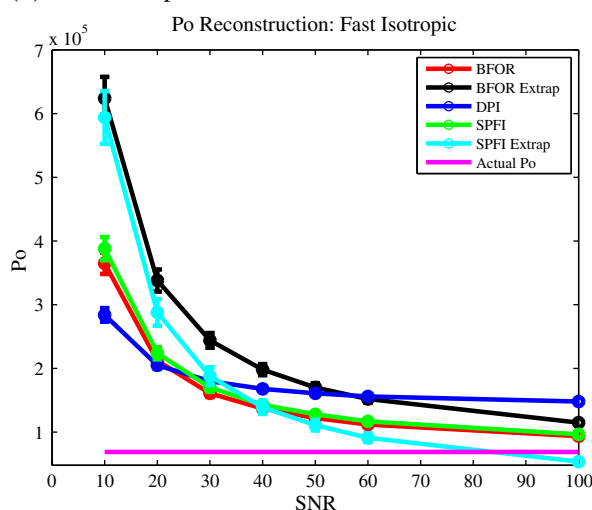
(a) Fast Anisotropic P_o



(b) Slow Anisotropic P_o



(c) Fast Isotropic P_o



(d) Slow Isotropic P_o

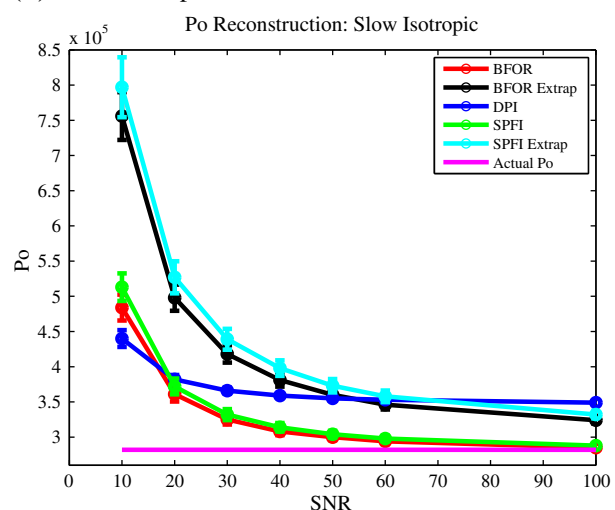


Fig. 7. Monte Carlo simulation investigating the effect of noise on estimation of P_o using fast/slow anisotropic components and fast/slow isotropic components. Error bars denote one standard deviation across 1000 trials.

only six measurements were acquired in this shell (see Table 1), which may be inadequate for their respective radial bases.

Performances of BFOR, DPI, and SPFI in reconstructing EAP. Fig. 4 shows the EAP reconstruction for the fast diffusion component across propagator space using each method. Modeling the fast component (i.e. head of the bi-exponential in Fig. 2) is tantamount to fitting a mono-exponential curve, and so the EAP reconstruction for the fast diffusion component can be viewed as if the diffusion signal decay was mono-exponential. Both BFOR and SPFI model the fast component EAP very well, accurately capturing the geometry and orientation of the EAP profile, and the BFOR reconstruction is nearly identical to that of SPFI. DPI performs reasonably well, but tends to overestimate the EAP.

Fig. 5 shows the EAP reconstruction for the slow diffusion component, which can be viewed as modeling the tail of the bi-exponential curve in Fig. 2. Note that the BFOR and SPFI reconstructions are quite alike. At $p = 1 \mu\text{m}$, all three methods capture the correct geometry of the ground truth EAP profile, but underestimate it, DPI more so. At $p = 5 \mu\text{m}$, all three methods are unsuccessful in capturing the correct geometry, in particular failing to capture the peaks of the ground truth EAP profile. However, they do capture the correct orientation. At $p = 10$ and especially $p = 15 \mu\text{m}$, the BFOR and SPFI EAP

reconstructions of the slow diffusion component begin to suffer from Gibbs ringing, which arise from the truncation of the signal bases at high q . The DPI reconstruction at $p = 15 \mu\text{m}$ benefits from the inherent smoothing of Laplacian signal modeling, with no spurious peaks present. Although oversmoothed and overestimated, it does a much better job than BFOR and SPFI in resolving the correct fiber orientation at $p = 15 \mu\text{m}$. The difficulty in reconstructing the EAP for the slow diffusion component is due to the slow diffusion component being sensitive to truncation effects. The reality of finite sampling makes it challenging to capture the tail of the bi-exponential curve. How then should one combat the effects of truncation artifacts?

Signal extrapolation. Extrapolating the diffusion signal to higher q -values so that q -space is more thoroughly explored could mitigate the truncation effects. Signal extrapolation can increase the spatial resolution of the EAP (Cohen and Assaf, 2002), and in the case of DSI, significantly reduce the cumbersome q -space sampling (Yeh et al., 2008). By linearly damping the signal measurements in the outermost shell ($b = 9375$ shell), we were able to (linearly) extrapolate samples onto three new ‘pseudo-shells.’ Specifically, the outermost signal measurements were attenuated by a factor of 0.7, 0.4, and 0.1 to form the three ‘pseudo-shells.’ The BFOR and SPFI scaling factors, τ and ζ , respectively, were changed for the extrapolation to

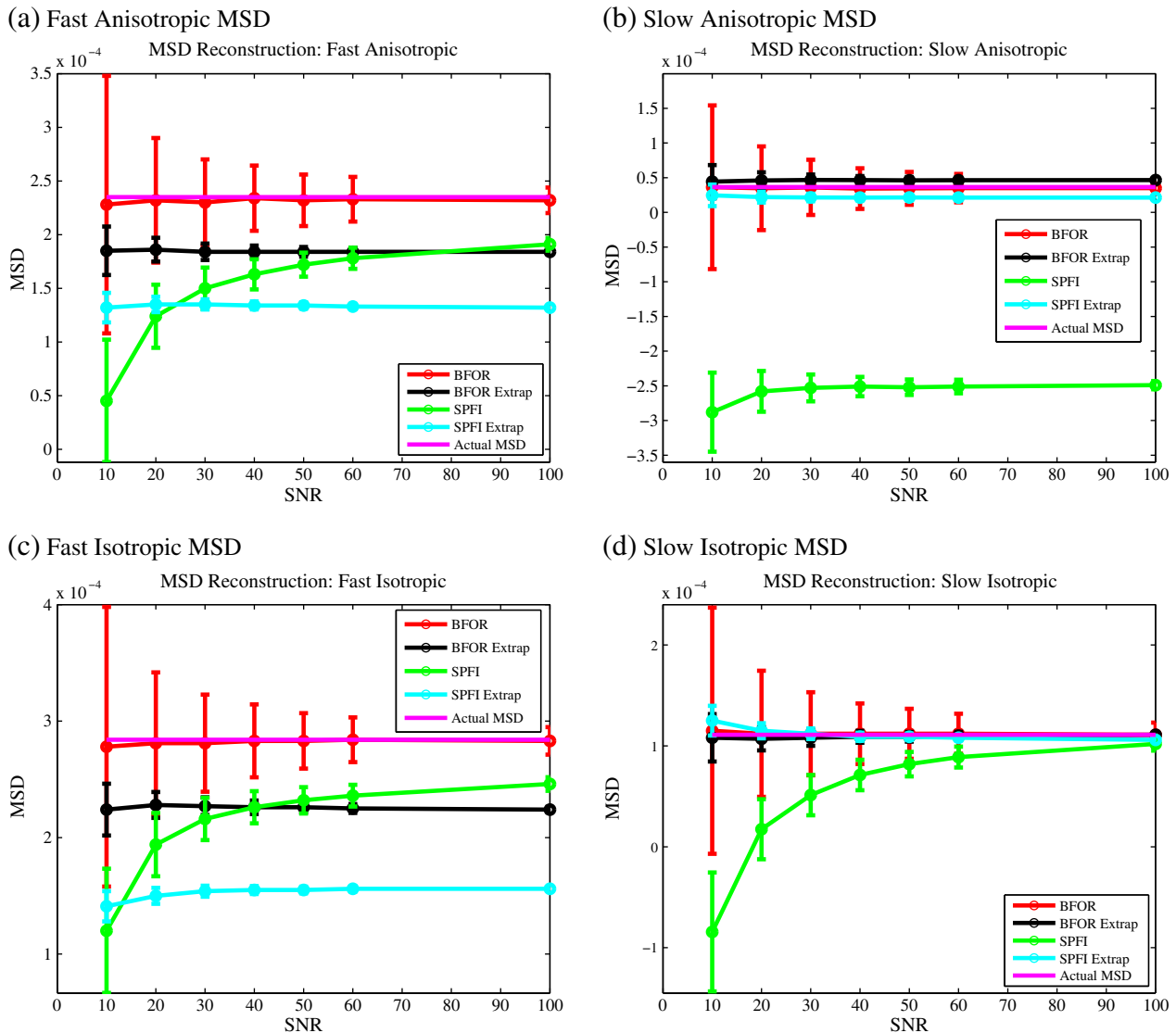


Fig. 8. Monte Carlo simulation investigating the effect of noise on estimation of MSD using fast/slow anisotropic components and fast/slow isotropic components. Error bars denote one standard deviation across 1000 trials.

$\tau = 136.8 \text{ mm}^{-1}$ and $\zeta = 1100$. Note that the q -space sampling interval Δq was not changed for the extrapolation.

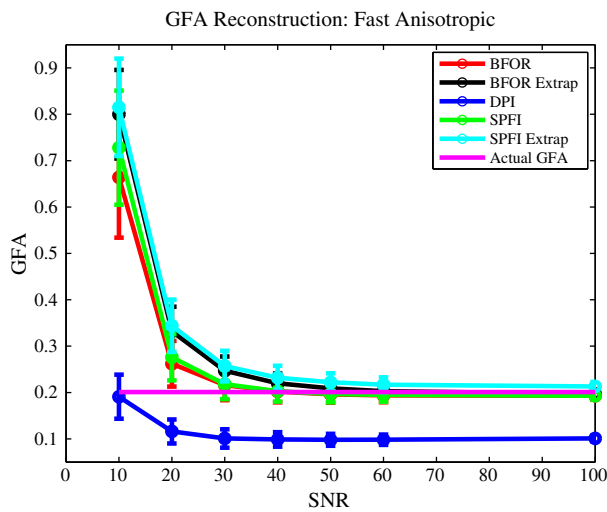
Fig. 6 shows that signal extrapolation improves the reconstruction of the slow EAP component for both BFOR and SPFI. At $p = 10 \text{ }\mu\text{m}$, the BFOR and SPFI slow EAP reconstructions with signal extrapolation, although not perfectly capturing the ground truth geometry, better capture the angular features of the ground truth than those without signal extrapolation. The biggest improvement, however, is seen at $p = 15 \text{ }\mu\text{m}$, where the pronounced Gibbs ringing is greatly reduced by the signal extrapolation. In particular, the BFOR and SPFI slow EAP reconstructions with signal extrapolation at $p = 15 \text{ }\mu\text{m}$ are not spiky and much closer to the ground truth, although their orientations are slightly off, than those without extrapolation (Fig. 5). Note that both the BFOR and SPFI slow EAP reconstructions with extrapolation are quite alike. The BFOR fast EAP reconstruction was not affected by extrapolation, being nearly identical to its counterpart without extrapolation. However, the SPFI fast EAP reconstruction with extrapolation was moderately less accurate than that without extrapolation. In general, signal extrapolation can significantly improve EAP reconstructions at larger diffusion displacements (i.e. $p = 15 \text{ }\mu\text{m}$).

Estimation of q -space indices. Fig. 7 shows the results for the P_0 measurements. Without signal extrapolation, BFOR and SPFI asymptotically approach the ground truth fast anisotropic P_0 , whereas DPI overestimates it. All three methods, without signal extrapolation, severely underestimate slow anisotropic P_0 , which is due to the truncation of the signal bases at high q . Both BFOR and SPFI asymptotically approach the ground truth fast/slow isotropic P_0 , while DPI overestimates both. At low levels of SNR (e.g. 10 and 20), which is quite common in diffusion MRI, all three methods (without signal extrapolation) have biased estimates of P_0 , though the variance is fairly small.

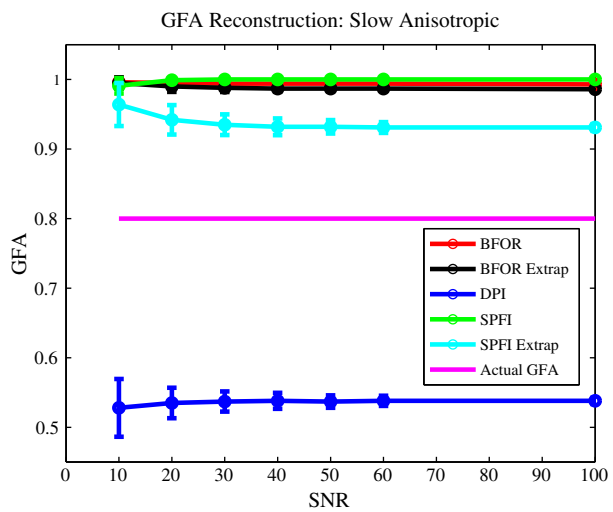
When signal extrapolation is applied, the estimation of the slow anisotropic P_0 by BFOR and SPFI significantly improves, as shown in Fig. 7b. According to Fig. 7a, signal extrapolation does not asymptotically affect SPFI's estimation of fast anisotropic P_0 , but slightly worsens that of BFOR's. At low levels of SNR, however, signal extrapolation results in more severe overestimation of fast anisotropic P_0 than without signal extrapolation for both BFOR and SPFI.

Fig. 8 shows the results for the MSD measurements. BFOR estimates both the fast and slow anisotropic/isotropic MSD very well across SNR levels. However, at low levels of SNR, the variability (given by the standard deviation) of the BFOR estimation of MSD is

(a) Fast Anisotropic GFA



(b) Slow Anisotropic GFA



(c) Isotropic GFA

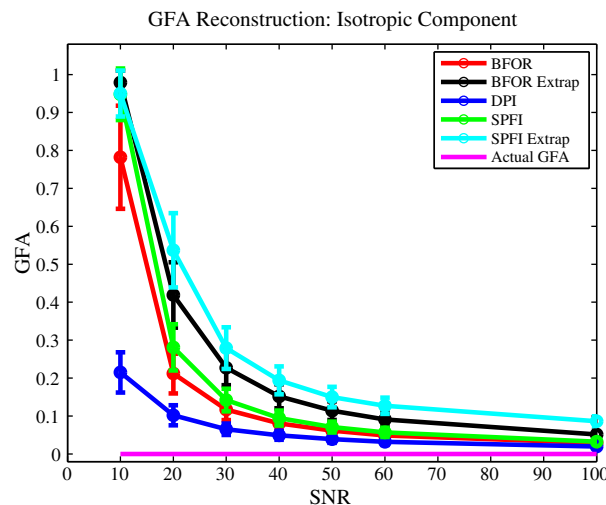


Fig. 9. Monte Carlo simulation investigating the effect of noise on estimation of GFA using fast/slow anisotropic components and an isotropic component. GFA was computed at $p = 10 \text{ }\mu\text{m}$. Error bars denote one standard deviation across 1000 trials.

quite large, indicating strong sensitivity to noise. SPFI without signal extrapolation severely underestimates anisotropic MSD, giving negative values for slow anisotropic MSD, which indicates that it will give inaccurate measurements of the MSD of WM. SPFI also underestimates fast isotropic MSD, but asymptotically approaches ground truth slow isotropic MSD. Interestingly, there is less variability in SPFI's estimation of MSD than BFOR.

When signal extrapolation is applied to the MSD measurements, SPFI's estimations of slow anisotropic and slow isotropic MSD significantly improve, well-estimating them across SNR levels, as shown in Figs. 8b and d, respectively. Specifically, the SPFI slow anisotropic MSD estimation is no longer negative with signal extrapolation. BFOR's estimations of slow anisotropic and slow isotropic MSD with extrapolation are nearly identical to those without it. However, the variability of the BFOR and SPFI MSD measurements is much less than those without extrapolation. A negative consequence of signal extrapolation is that it increases the inaccuracy (i.e. asymptotically worsening) of the BFOR/SPFI fast anisotropic and fast isotropic MSD estimations, all of which are greatly underestimated. The simulations indicate signal extrapolation may be more beneficial to SPFI's estimation of MSD than that of BFOR's.

Fig. 9 shows the results for the GFA measurements. Asymptotically, BFOR and SPFI without signal extrapolation approach the ground truth fast anisotropic GFA, while DPI underestimates it. Across SNR levels, DPI severely underestimates slow anisotropic GFA, while both BFOR and SPFI greatly overestimate it. For the case of isotropic diffusion, where $GFA = 0$, the GFA estimated by each method approaches zero at high SNR. However, at $SNR = 10$, both SPFI and BFOR severely overestimate the isotropic GFA, giving values comparable to the GFA of WM. DPI's estimation of the isotropic component is more robust to noise than BFOR and SPFI.

SPFI with signal extrapolation still overestimates slow anisotropic GFA, though slightly less so than without it, but the extrapolation increases the estimation's variability at the same time. Signal extrapolation has negligible effects on BFOR's estimation of slow anisotropic GFA. Both BFOR's and SPFI's estimation of fast anisotropic GFA are

not asymptotically affected by signal extrapolation, having similar convergences as those without signal extrapolation, but the extrapolation causes both methods to overestimate fast anisotropic GFA to a larger degree at $SNR = 10, 20$, and 30 than without it. Based on Fig. 9c, both SPFI and BFOR with signal extrapolation overestimate isotropic GFA, across SNR levels, to a larger extent than without extrapolation, implying that extrapolation is quite sensitive to noise in CSF regions.

Results of human brain data

Resolving single fibers. In Fig. 10, a 4×4 ROI was drawn on the splenium of corpus callosum. The EAP profiles reconstructed at $p = 10 \mu m$ by each method have the fundamental peanut shape of a single fiber. Note that the BFOR and SPFI reconstructions in both cases are very similar. We see that application of smoothing $t = 550$ removes the center peaks of the BFOR EAP profiles. Whether these center peaks in the EAP profiles are the result of Gibbs ringing (i.e. artificial peaks) or describe some underlying biological process is an open question.

Resolving crossing fibers. In Fig. 11, a 4×9 ROI was drawn in a region of fiber crossing, where the EAP profiles were reconstructed at $p = 10 \mu m$. Although not identical, the BFOR and SPFI reconstructions are quite similar, and they recover and well discriminate crossing fiber configurations in the EAP. DPI, however, tends to oversmooth the EAP profiles of crossing WM fibers, resulting in spherical/oblate shapes that give the impression of isotropic diffusion. Based on Fig. 11d, the application of smoothing $t = 60$ to BFOR removes the center peaks from several voxels, but at the expense of slight angular smoothening of EAP profiles themselves.

Fig. 12 shows the reconstructed EAP profiles for the same crossing fiber region, but at $p = 15 \mu m$. Fiber crossing configurations are recovered and well discriminated in the EAP for each method. Unlike at $p = 10 \mu m$, the DPI EAP reconstruction at $p = 15 \mu m$ is sharper and does not suffer from oversmoothering. In fact, as the propagator radius p increases, the angular resolution improves, at the expense of the EAP profiles becoming spiky, as is evident in Figs. 12a, e, and g. When a smoothing of $t = 60$ is applied to the BFOR EAP reconstruction

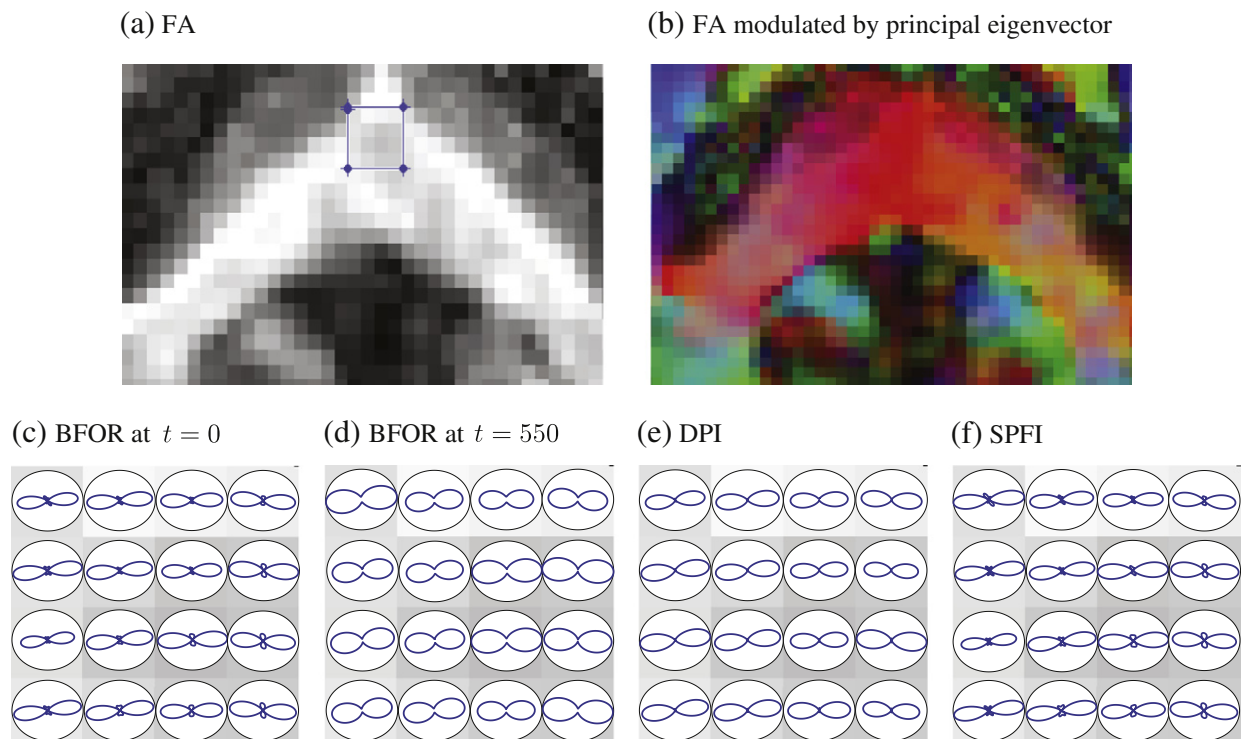


Fig. 10. Axial slice of FA map of adult human brain at $b = 1500 \text{ s/mm}^2$ (second shell), where 4×4 ROI is drawn on splenium of corpus callosum. Plotted is the EAP profile at $p = 10 \mu m$ overlaid on FA map in 4×4 ROI using BFOR at (c) $t = 0$, (d) $t = 550$, and (e) DPI and (f) SPFI.

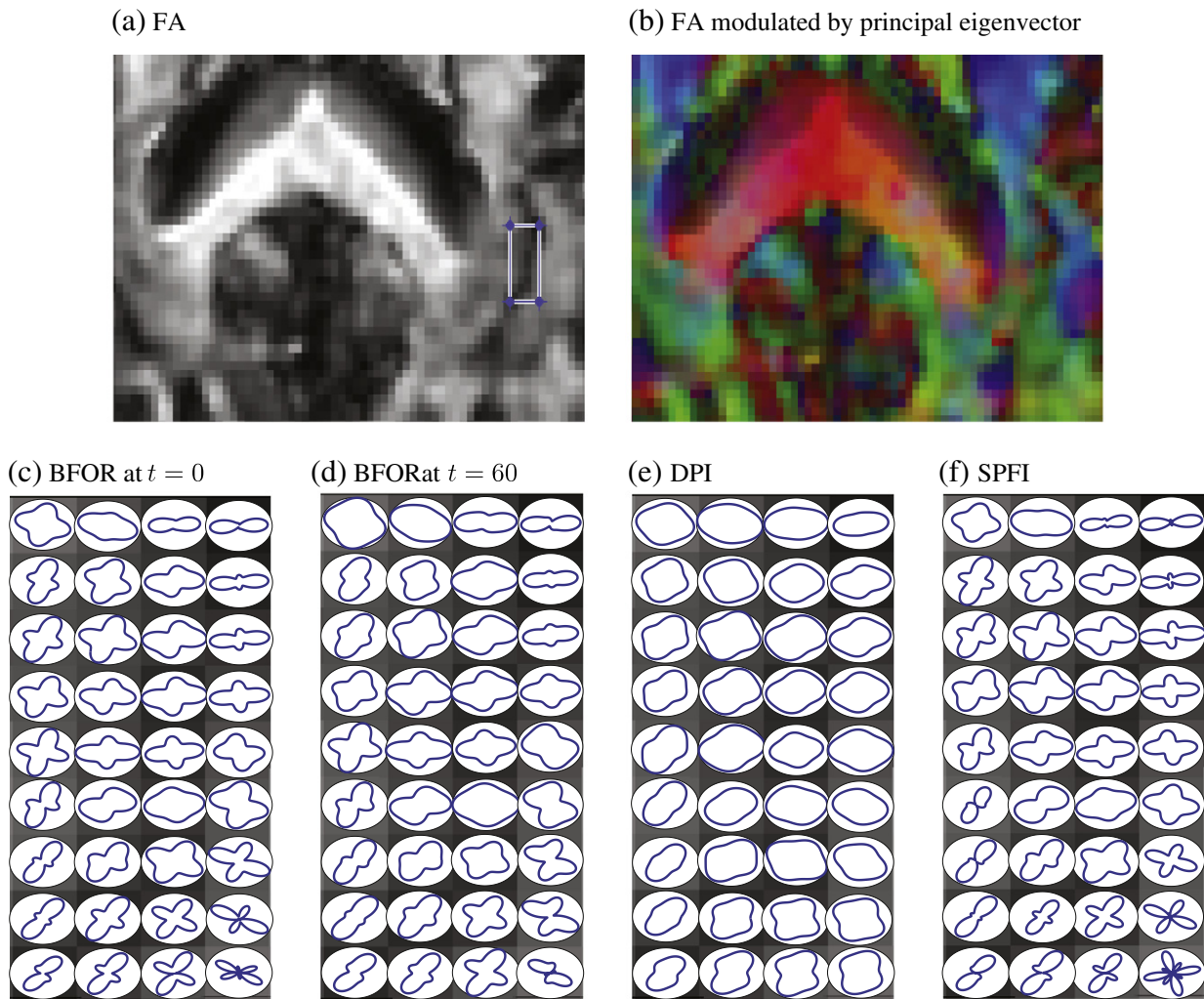


Fig. 11. Axial slice of FA map of adult human brain at $b = 1500 \text{ s/mm}^2$ (second shell), where a 4×9 ROI is drawn on a region of crossing fibers. Plotted is the EAP profile at $p = 10 \mu\text{m}$ overlaid on FA map in 4×9 ROI using (c) BFOR at $t = 0$, (d) $t = 60$, and (e) DPI and (f) SPFI. The splenium is to the left of the ROI.

(without signal extrapolation), the subsequent EAP profiles are still spiky. At $t = 350$, the spikiness is smoothed out, but many of the WM voxels have EAP reconstructions significantly differing, with respect to orientation and geometry, from those at $t = 0$. Figs. 12d and f show the BFOR and SPFI EAP profiles reconstructed at $p = 15 \mu\text{m}$ with signal extrapolation, respectively, which are much less spiky than the corresponding ones without signal extrapolation, which is consistent with the synthetic results shown in Fig. 6. The signal extrapolation also smoothes the reconstructed EAP profiles, but unlike BFOR at $t = 350$, none of the WM voxels are oversmoothed to such a degree that their EAP profiles have oblate shapes. Unlike BFOR at $t = 350$, the underlying EAP geometry and orientation of the BFOR/SPFI reconstructions with signal extrapolation are fairly consistent to those without extrapolation (at $t = 0$). As observed at $p = 10 \mu\text{m}$, the BFOR and SPFI EAP reconstructions at $p = 15 \mu\text{m}$ are quite similar, which is consistent with the synthetic data results.

Q-space indices. Table 3 shows the mean index value and corresponding standard deviation for genu and splenium of corpus callosum (WM) and putamen (GM). Three 4×4 ROIs were drawn on both the genu and splenium and one such ROI on both the left and right putamen, across several slices. The table shows that the SPFI MSD (without signal extrapolation) erroneously gives negative values for the MSD of genu and splenium. With extrapolation, the SPFI MSD of genu and splenium are positive.

Based on the numerical simulations, signal extrapolation was applied to both BFOR's and SPFI's estimation of P_0 . Fig. 13 displays

an axial slice of P_0 generated by each method. In the first row, we show P_0 computed from BFOR, SPFI, DPI, and numerically (Wu et al., 2008). The BFOR, SPFI, and numerical P_0 maps are quite similar, exhibiting rich GM/WM and tissue/CSF contrasts while the DPI P_0 map has less GM/WM contrast. In particular, based on Table 3, the P_0 ratio of WM to GM is slightly above 2 for BFOR and SPFI, while less than 2 for DPI.

The MSD maps computed from BFOR, SPFI, DPI, and numerically (Wu et al., 2008) are shown in Fig. 14. Both the BFOR and numerical MSD maps exhibit rich tissue/CSF contrast, but have little WM/GM contrast, which is similar to the DTI MD. Table 3 shows that the BFOR MSD values for WM and GM are quite similar. In the SPFI (without signal extrapolation) MSD map, WM regions are completely dark, having negative MSD values. This is consistent with the results of the noise simulations, which showed that SPFI severely underestimates the MSD of WM. Signal extrapolation has the effect of enforcing the positivity constraint on the MSD for SPFI. However, both the BFOR and SPFI MSD maps with signal extrapolation have poor tissue/CSF contrast because of the noise induced by the signal extrapolation. With regards to BFOR, both the synthetic and *in vivo* data suggest that it's best not to use signal extrapolation in estimating MSD. SPFI, however, does not generate reliable MSD maps either with or without signal extrapolation. Although DPI predicts the MSD to be zero, an MSD map was computed for it by numerically estimating the second moment of the diffusion propagator. The contrast of the MSD DPI map is completely inverted, with WM appearing bright and CSF dark.

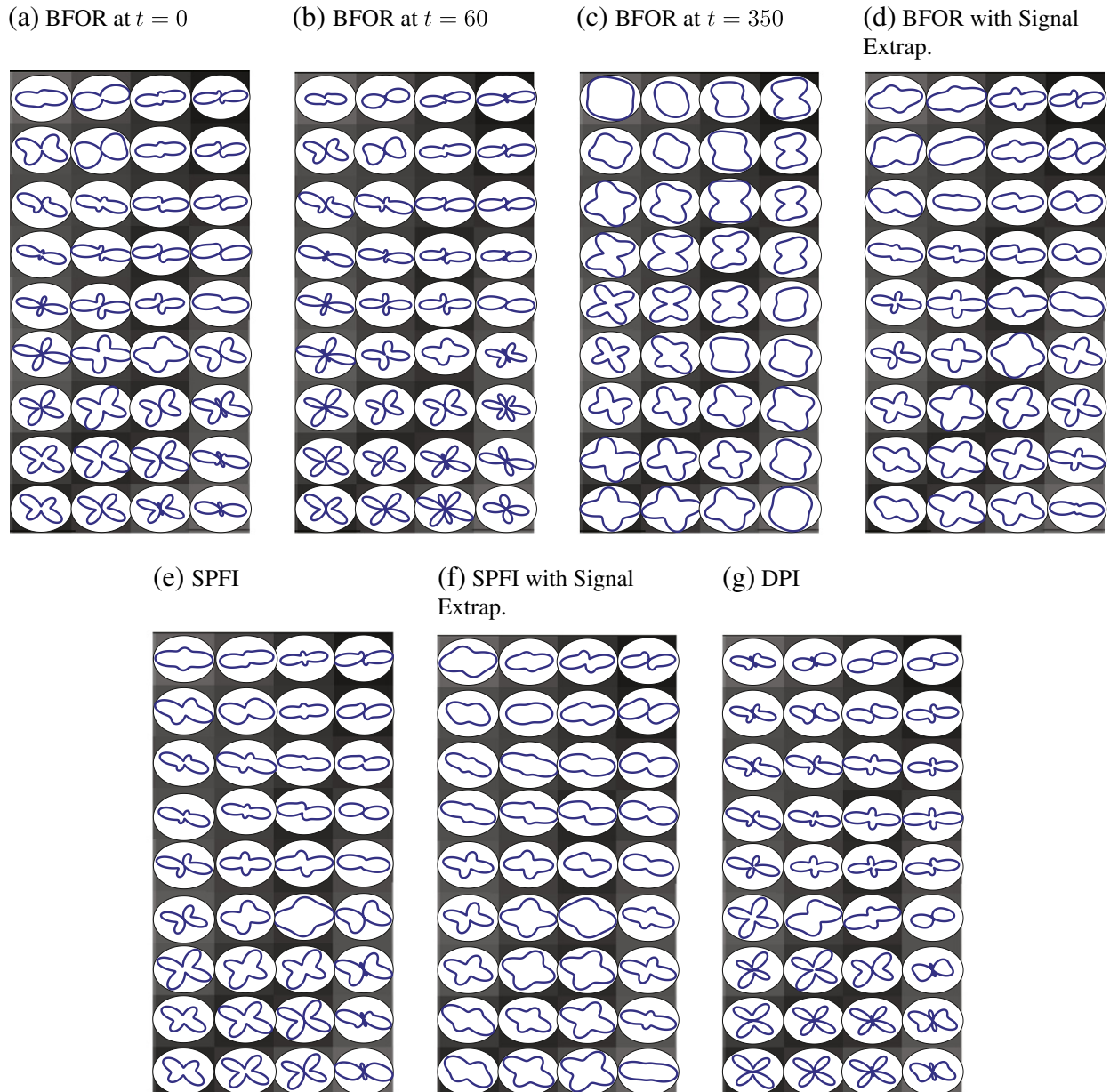


Fig. 12. EAP profiles reconstructed at $p = 15 \mu\text{m}$ for same crossing fiber region shown in Fig. 11.

Fig. 16 displays axial slices of the GFA computed at $p = 5, 10,$ and $15 \mu\text{m}$ for each method, illustrating how the anisotropy of different WM regions, such as the corpus callosum and capsules, varies with diffusion displacement p . According to Table 3, at $p = 5 \mu\text{m}$, the anisotropy of corpus callosum is lower with respect to levels seen in DTI. At $p = 10 \mu\text{m}$, the corpus callosum is very anisotropic, as can be seen from Table 3, indicating that $p = 10 \mu\text{m}$ is a diffusion displacement worth reconstructing the EAP at. The GFA at $p = 15 \mu\text{m}$ is more noisy, which is due to truncation of signal basis at high q -values and $15 \mu\text{m}$ being well beyond the resolvable resolution (of diffusion displacement) limit. The BFOR and SPFI GFA maps without signal extrapolation are very similar, while WM regions in the DPI computed GFA maps at $p = 5$ and $10 \mu\text{m}$ have lower intensity than those of BFOR and SPFI, which is consistent with the underestimation of GFA(10) by DPI observed in the Monte Carlo noise simulations (Fig. 9). CSF regions in the BFOR GFA(10) map with signal extrapolation are more noisy than without it, which is consistent with the simulation results shown in Fig. 9c. In the case of SPFI, however, the noise

level is very severe in CSF regions in the GFA(5) and GFA(10) maps with signal extrapolation than those without it.

Discussion

The three analytical EAP reconstruction schemes examined in this paper possess both certain advantages and disadvantages. Among the three, the DPI reconstruction uses the least number of expansion coefficients. According to both synthetic and *in vivo* data, DPI tends to greatly oversmooth the EAP, especially $p = 10 \mu\text{m}$, but performs well at $p = 15 \mu\text{m}$ where it did not make use of signal extrapolation. DPI's assumption of Laplacian signal modeling, however, entails that the MSD is zero (refer to Eq. (14)). Fig. 9 indicates that DPI greatly underestimates GFA(10), which is reflected in Fig. 16 and Table 3. In addition, the DPI signal basis is only applicable at $q > 0$, which is unrealistic since the diffusion signal is defined at $q = 0$.

The SPFI signal basis possesses several advantages in that it radially decays to zero and has no singularity at $q = 0$. In addition, the EAP

Table 3
Values of indices for various WM and GM structures.

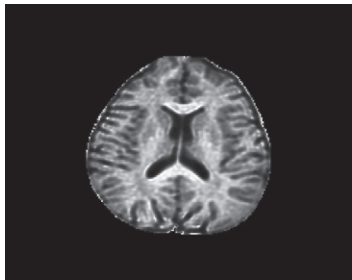
Index	Splenium	Genu	Putamen
BFOR GFA(5)	0.212 ± 0.0162	0.188 ± 0.0153	0.0353 ± 0.0130
BFOR GFA(5) Extrap	0.416 ± 0.0310	0.370 ± 0.0325	0.0879 ± 0.0296
SPFI GFA(5)	0.234 ± 0.0178	0.209 ± 0.0179	0.0424 ± 0.0152
SPFI GFA(5) Extrap	0.461 ± 0.0342	0.402 ± 0.0387	0.103 ± 0.0342
DPI GFA(5)	0.129 ± 0.00849	0.111 ± 0.0103	0.0166 ± 0.00642
BFOR GFA(10)	0.998 ± 0.00310	0.991 ± 0.0184	0.254 ± 0.0686
BFOR GFA(10) Extrap	0.999 ± 0.00270	0.991 ± 0.0187	0.360 ± 0.0759
SPFI GFA(10)	0.999 ± 0.00246	0.994 ± 0.0156	0.263 ± 0.0735
SPFI GFA(10) Extrap	0.996 ± 0.00535	0.988 ± 0.0243	0.339 ± 0.0722
DPI GFA(10)	0.831 ± 0.0280	0.766 ± 0.0533	0.123 ± 0.0380
BFOR GFA(15)	0.927 ± 0.0424	0.857 ± 0.0736	0.397 ± 0.0830
BFOR GFA(15) Extrap	0.859 ± 0.0782	0.753 ± 0.104	0.349 ± 0.0737
SPFI GFA(15)	0.957 ± 0.0346	0.875 ± 0.0849	0.380 ± 0.0797
SPFI GFA(15) Extrap	0.858 ± 0.0838	0.730 ± 0.104	0.318 ± 0.0722
DPI GFA(15)	0.952 ± 0.0253	0.906 ± 0.0566	0.286 ± 0.0682
BFOR MSD (10^{-3} mm ²)	0.207 ± 0.0860	0.219 ± 0.0980	0.211 ± 0.0820
BFOR MSD Extrap (10^{-3} mm ²)	0.137 ± 0.0300	0.162 ± 0.0330	0.158 ± 0.0160
SPFI MSD (10^{-3} mm ²)	-0.0670 ± 0.0770	-0.0220 ± 0.0950	0.0700 ± 0.0510
SPFI MSD Extrap (10^{-3} mm ²)	0.0830 ± 0.0210	0.103 ± 0.0210	0.137 ± 0.0150
DPI MSD (10^{-3} mm ²)	4.60 ± 0.430	4.27 ± 0.460	4.28 ± 0.361
BFOR P_0 (10^5 mm ⁻³)	6.63 ± 0.729	5.65 ± 0.630	2.95 ± 0.263
BFOR P_0 Extrap (10^5 mm ⁻³)	10.8 ± 1.17	9.24 ± 1.07	4.41 ± 0.396
SPFI P_0 (10^5 mm ⁻³)	7.00 ± 0.757	6.06 ± 0.649	3.12 ± 0.258
SPFI P_0 Extrap (10^5 mm ⁻³)	11.2 ± 1.33	9.37 ± 1.22	4.33 ± 0.449
DPI P_0 (10^5 mm ⁻³)	5.00 ± 0.514	4.38 ± 0.435	2.99 ± 0.231
BFOR QIV (10^{-10} mm ⁵)	4.04 ± 0.447	4.78 ± 0.563	11.1 ± 1.28

is derived via integration over the entire q -space, unlike BFOR and DPI, where the q -space integration is up to a certain bound that is related to q_{max} . Interestingly, however, the SPFI EAP reconstructions for both synthetic and real datasets are quite similar to those of BFOR, suggesting the two methods may be inherently related. According to the synthetic data, signal extrapolation greatly improves the SPFI EAP reconstruction at $p = 15 \mu\text{m}$. Although not shown in this paper, heat diffusion smoothing can be applied to SPFI. SPFI's estimation of P_0 and GFA, either with or without signal extrapolation, is quite comparable

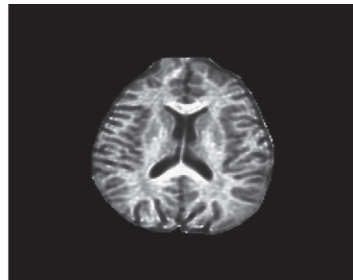
to those of BFOR's. However, it poorly estimates the MSD, which recalling Eq. (14), may be due to, from a computational standpoint, SPFI's signal basis not being an eigenfunction of the Laplacian operator.

The main limitation of the BFOR signal model, as mentioned in the Theory section, is that it infinitely oscillates about zero, which entails a finite integration of the signal over q -space (τ being the upperbound) to retrieve the EAP. However, based on Fig. 3, BFOR outperforms DPI and SPFI in modeling the diffusion signal. Heat diffusion smoothing helps in removing potentially spurious peaks, and signal extrapolation

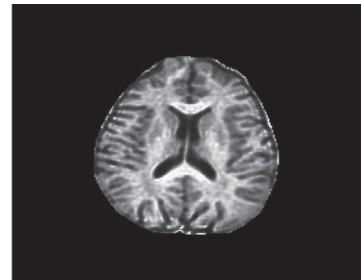
(a) BFOR



(b) BFOR with Signal Extrapolation



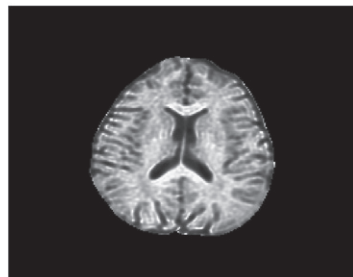
(c) SPFI



(d) SPFI with Signal Extrapolation



(e) DPI



(f) Numerical

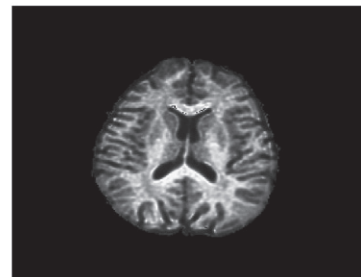


Fig. 13. Axial slice of P_0 generated by each method.

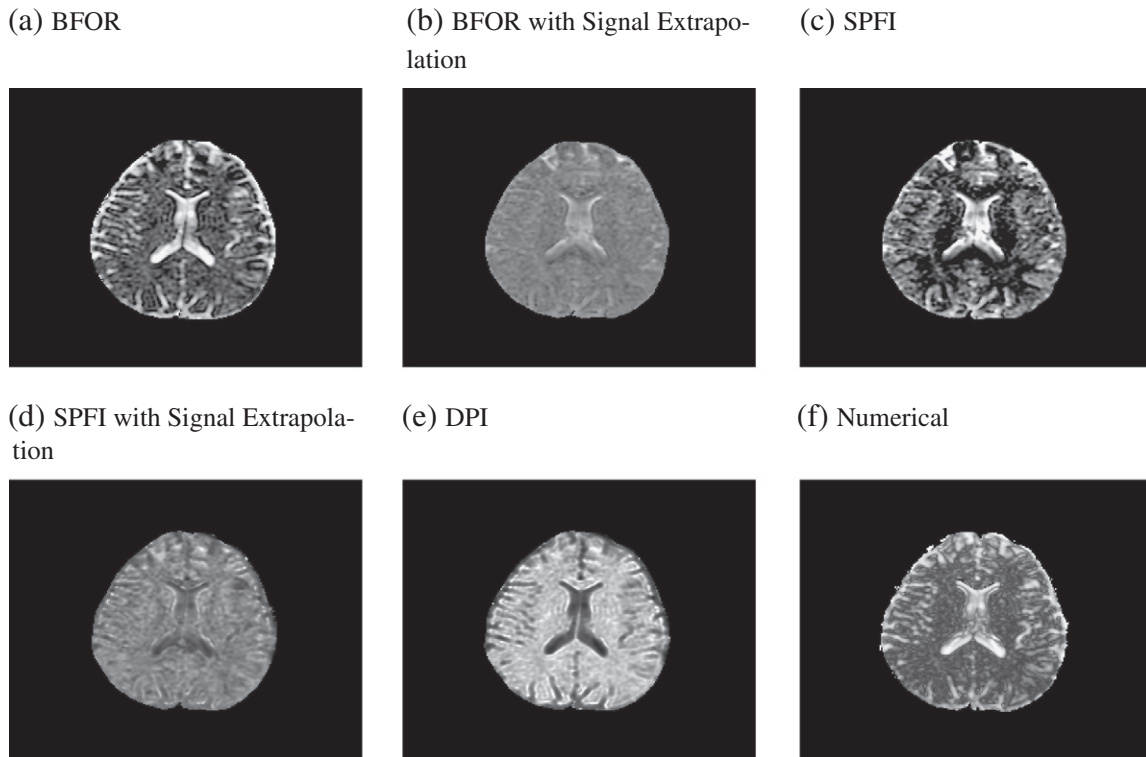


Fig. 14. Axial slice of MSD generated by each method.

significantly improves the EAP reconstruction at $p = 15 \mu\text{m}$. According to both the synthetic and real data, BFOR gives reasonable estimates of all three q -space indices.

The slow component of diffusion is the most sensitive to truncation artifacts, which can induce severe Gibbs ringing and adversely affect the orientation of reconstructed EAP. In this paper, signal extrapolation was proposed as a means to mitigate the effects of such artifacts, and was observed to be most effective at higher radii (i.e. $p = 15 \mu\text{m}$), where the effects of signal truncation artifacts are most pronounced. The significant improvement in the BFOR/SPFI EAP reconstruction at $p = 15 \mu\text{m}$ via linear signal extrapolation hence suggests that extrapolation may be a useful preprocessing step for EAP reconstruction at large diffusion displacements. Signal extrapolation also greatly improves the accuracy of the BFOR/SPFI P_0 estimation, according to the synthetic data. However, signal extrapolation increases the severity of noise in CSF regions in the GFA and MSD maps for both BFOR and SPFI, as evidenced by the

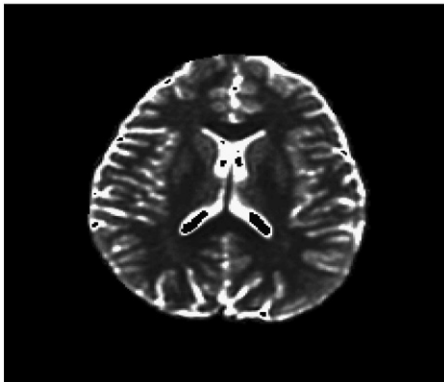


Fig. 15. Axial slice of BFOR QIV. Within the CSF regions, some voxels were zeroed out because they blew up upon the division operation in computing QIV.

synthetic and real datasets, reducing tissue/CSF contrast. Hence, extrapolation may not be desirable for GFA and MSD estimation. Future work includes optimizing the signal extrapolation for a given signal basis.

The degree of heat diffusion smoothing desired depends on the propagator radius and whether the fibers are single or crossing. Based on Fig. 10, a smoothing of $t = 550$ was applied to splenium at $p = 10 \mu\text{m}$ to remove the center peaks. However, for a crossing fiber region at $p = 10 \mu\text{m}$, a smoothing of $t = 60$ was only applied because the EAP profiles of crossing fibers can easily become oversmoothed, resulting in oblate shapes. The fact that the smoothing factor is different for different brain regions poses a problem for whole brain EAP processing. One way to address this issue is to use an optimal bandwidth selection framework from statistics to estimate the optimal t . Specifically, the bandwidth t is selected to minimize a certain cost function. In a spline setting, the cost function will be a generalized cross-validation (GCV) criterion (Katkovnik, 1999). In a more simple setting like ours, we can choose the t that minimizes the sum of the squared residuals, where the residual is simply the difference between the actual data and model fit.

Although the encoding scheme in this study consisted of equally spaced concentric spherical shells, the BFOR framework does not require such a scheme. BFOR only requires a minimum of two diffusion weightings and use of a spherical coordinate system. Random sampling along q -space or even the use of unequally spaced concentric shells is perfectly valid. This, however, leads to the important question of what is the best way to sample N diffusion measurements in q -space, which have started to be addressed (Assemlal et al., 2009b; Caruyer et al., 2011; Merlet et al., 2011). Future work includes optimizing the q -space sampling and applying compressed sensing to BFOR.

Both the ODF and EAP profiles are not sharp enough to extract the true fiber orientation. Rather, the fiber orientation is given by the fiber orientation distribution function (fODF), which can be computed via spherical deconvolution of some assumed kernel (i.e. response

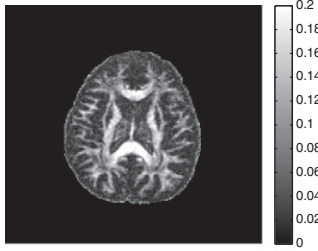
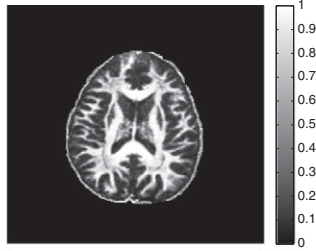
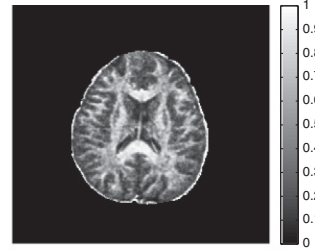
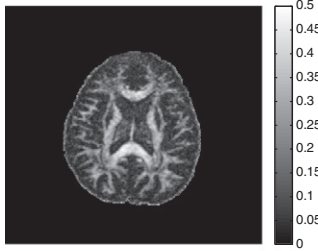
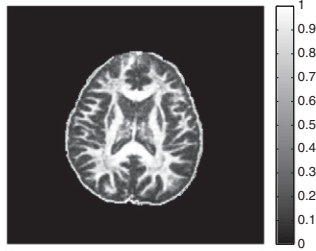
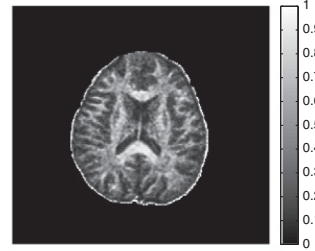
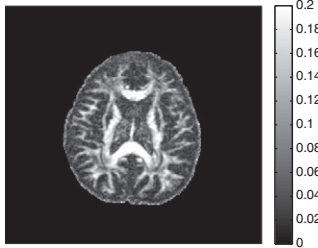
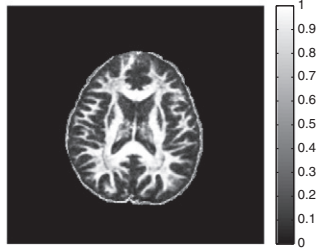
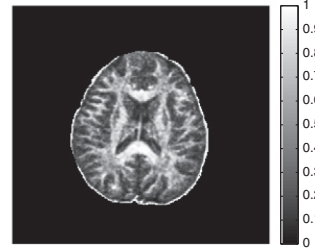
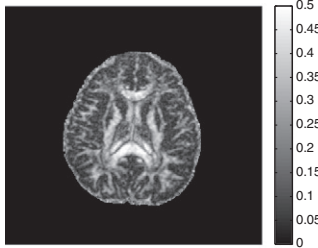
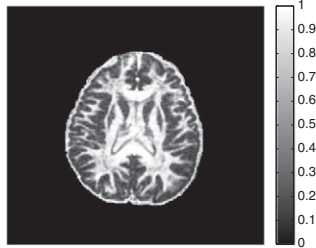
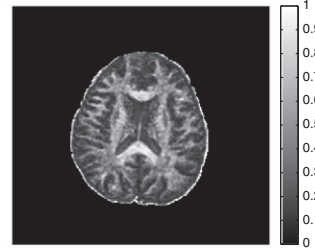
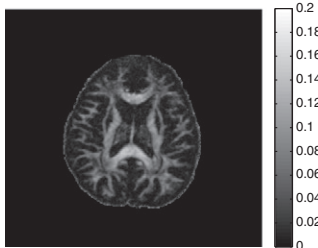
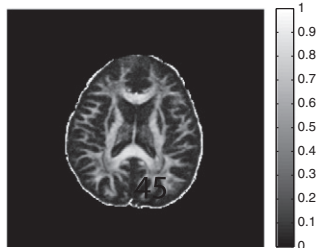
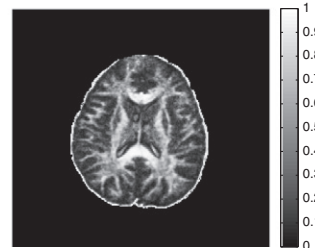
BFOR(a) $p = 5 \mu\text{m}$ (b) $p = 10 \mu\text{m}$ (c) $p = 15 \mu\text{m}$ **BFOR with Signal Extrapolation**(d) $p = 5 \mu\text{m}$ (e) $p = 10 \mu\text{m}$ (f) $p = 15 \mu\text{m}$ **SPFI**(g) $p = 5 \mu\text{m}$ (h) $p = 10 \mu\text{m}$ (i) $p = 15 \mu\text{m}$ **SPFI with Signal Extrapolation**(j) $p = 5 \mu\text{m}$ (k) $p = 10 \mu\text{m}$ (l) $p = 15 \mu\text{m}$ **DPI**(m) $p = 5 \mu\text{m}$ (n) $p = 10 \mu\text{m}$ (o) $p = 15 \mu\text{m}$ 

Fig. 16. GFA maps computed at $p = 5, 10$, and $15 \mu\text{m}$.

function) from q -space diffusion signal (Tournier et al., 2004). Mathematically, the angular convolution is given by

$$E(q, \mathbf{u}) = \int_{S^2} F(\mathbf{r}) K(q, \mathbf{u}, \mathbf{r}) d^2 \mathbf{r}, \quad (20)$$

where $F(\mathbf{r})$ is the fODF and K the kernel. The derivation of the fODF using the BFOR, SPFI, and DPI signal bases is worth exploring in the future.

In any future clinical study employing HYDI to examine brain pathology, where rotationally invariant indices like GFA and P_0 can be used to assess changes between diseased and normal subjects, voxel-wise analysis is desired. However, spatial normalization of multiple b-value datasets is no easy task. Recently, the authors in Du et al. (2012) proposed a registration algorithm to align HARDI datasets using the ODFs. Specifically, the algorithm seeks an optimal diffeomorphism of large deformation between two ODF fields across a spatial volume domain and at the same time, locally reorients an ODF in a manner consistent with the underlying anatomical structure. HYDI images could be aligned using the same algorithm, except replacing the ODF with the EAP.

The MSD measure is quite sensitive to noise (Assaf and Cohen, 2000; Wu and Alexander, 2007). The authors in Wu et al. (2008) proposed an alternative measure to MSD called the q -space inverse variance (QIV), which is a pseudo-diffusivity measure. Mathematically, the QIV is defined as

$$QIV = \left[\int q^2 E(\mathbf{q}) d^3 \mathbf{q} \right]^{-1} \quad (21)$$

The QIV can thus be interpreted as the inverse of the “variance” of q (i.e. $QIV = 1/\langle q^2 \rangle$). It is not a real variance in the statistical sense because $E(\mathbf{q})$ does not constitute a probability density function. The QIV is not an arbitrary measure, but related to the EAP in a manner analogous to which the MSD is related to the diffusion signal—in Appendix F, we will show that

$$QIV^{-1} = \frac{-\nabla^2 P(\mathbf{p})|_{p=0}}{4\pi^2}. \quad (22)$$

The QIV within the BFOR framework is (see Appendix F for derivation)

$$QIV_{\text{BFOR}} = \frac{1}{2\sqrt{\pi}\tau^5 \sum_{n=1}^N (-1)^n C_{n1} \frac{(6-\alpha_{n0}^2)}{\alpha_{n0}^4}} \quad (23)$$

Fig. 15 displays an axial slice of the BFOR QIV, illustrating rich tissue/CSF contrast. The tissue/CSF contrast in the QIV is more enhanced than that of the MSD, and unlike the MSD, the QIV map also exhibits WM/GM contrast (the right and left putamen are visible in Fig. 15 but not in the MSD maps). According to Table 3, the QIV of the corpus callosum is about a third of that of the putamen.

Conclusion

We have introduced a new orthonormal basis to model the q -space diffusion signal and from which the EAP can be analytically reconstructed using hybrid, non-Cartesian sampling with multiple q -shell measurements. BFOR is a linear and efficient reconstruction based on heat equation estimation of the diffusion signal. Compared to DSI, BFOR employs much fewer diffusion measurements. Rotationally invariant q -space indices such as GFA, P_0 , and MSD can then be obtained using the derived EAP.

Acknowledgments

This study was supported by grants from the NIH (MH084051, MH062015, HD003352, and AG037639) and from the National Multiple Sclerosis Society (Translational Research Partnership Grant). The authors are thankful to Cheng Guan Koay and Steve Keckskemeti of the University of Wisconsin-Madison for insightful discussions on the estimation of the diffusion propagator.

Appendix A. Derivation of BFOR signal basis

We want to solve the following boundary value partial differential equation:

$$\left[\frac{1}{q^2} \frac{\partial}{\partial q} \left(q^2 \frac{\partial}{\partial q} \right) + \frac{1}{q^2 \sin \theta} \frac{\partial}{\partial \theta} \left(\sin \theta \frac{\partial}{\partial \theta} \right) + \frac{1}{q^2 \sin^2 \theta} \frac{\partial^2}{\partial \phi^2} \right] \psi_i(\mathbf{q}) = -\lambda_i \psi_i(\mathbf{q}), \quad \psi(q = \tau, \theta, \phi) = 0 \quad (A.1)$$

where we require $\lambda > 0$. Substituting the separable solution of the form

$$\psi(q, \theta, \phi) = f(q)h(\theta, \phi) \quad (A.2)$$

into Eq. (A.1), we obtain

$$q^2 \frac{d^2}{dq^2} f + 2q \frac{d}{dq} f + q^2 \lambda = -\frac{\Delta_{LB} h}{h} = l(l+1), \quad (A.3)$$

where $\Delta_{LB} = \frac{1}{\sin \theta} \frac{\partial}{\partial \theta} \left(\sin \theta \frac{\partial}{\partial \theta} \right) + \frac{1}{\sin^2 \theta} \frac{\partial^2}{\partial \phi^2}$ is the Laplace–Bertrami operator and l is some real-valued constant.

We first solve for the second equation in Eq. (A.3):

$$\Delta_{LB} h + l(l+1)h = 0 \quad (A.4)$$

The solutions to Eq. (A.4) are the spherical harmonics (SH) $Y_l^m(\theta, \phi)$.

The second equation in (A.3) can be written as

$$q^2 \frac{d^2}{dq^2} f + 2q \frac{d}{dq} f + [q^2 \lambda - l(l+1)] f = 0 \quad (A.5)$$

Defining a new variable $f(q) = \sqrt{\frac{\pi}{2\sqrt{\lambda}q}} F(q)$, we can transform Eq. (A.5) to

$$q^2 \frac{d^2}{dq^2} F + q \frac{d}{dq} F + [q^2 \lambda - (l+1/2)^2] F = 0, \quad (A.6)$$

which is simply a scaled version of the Bessel differential equation. The only bounded solution at the origin is given in terms of the Bessel function of the first kind as $F(q) = J_{l+1/2}(\sqrt{\lambda}q)$. The solution to Eq. (A.5) is then $f(q) = \sqrt{\frac{\pi}{2\sqrt{\lambda}q}} J_{l+1/2}(\sqrt{\lambda}q) = j_l(\sqrt{\lambda}q)$, where j_l is the spherical Bessel function of the first kind and we invoke the relation $J_l(x) = \sqrt{\frac{\pi}{2x}} J_{l+1/2}(x)$.

Imposing the boundary condition from Eq. (A.1), we have $j_l(\sqrt{\lambda}\tau) = 0$. Defining α_{nl} as the n th root of the l th order spherical Bessel function of first kind, then the eigenvalues are found to be $-\lambda_{nl} = -\frac{\alpha_{nl}^2}{\tau^2}$. Note that for $l=0$, the roots are simply $\alpha_{n0} = n\pi$.

Multiplying the spherical Bessel functions and the spherical harmonics together, we obtain the eigenfunctions (i.e. our orthonormal basis) to Eq. (A.1): $Z_{nlm}(q, \theta, \phi) = j_l(\sqrt{\lambda_{nl}q}) Y_l^m(\theta, \phi)$. Thus, the complete set of solutions to Eq. (A.1) is

$$\psi(q, \theta, \phi) \approx \sum_{n=1}^N \sum_{l=0}^L \sum_{m=-l}^l C_{nlm} j_l \left(\frac{\alpha_{nl} q}{\tau} \right) Y_l^m(\theta, \phi), \quad (A.7)$$

where N is the truncation order of the number of roots of spherical Bessel function and L the truncation order of the SH.

Now, to derive the diffusion signal, we make two important assumptions. First, we assume the diffusion signal $E(\mathbf{q})$ is a solution to the heat equation:

$$\nabla^2 E(\mathbf{q}, t) = \frac{\partial E}{\partial t}, \quad E(\mathbf{q}, t = 0) = H(\mathbf{q}), \quad (\text{A.8})$$

where $H(\mathbf{q})$ is simply the acquired signal. Second, we assume that the diffusion signal can be expressed as a linear combination of the orthonormal basis derived in Eq. (A.7):

$$E(q, \mathbf{u}, t) = \sum_{n=1}^N \sum_{l=0}^L \sum_{m=-l}^l C_{nlm} g_{nlm}(t) j_l\left(\frac{\alpha_{nl} q}{\tau}\right) Y_l^m(\mathbf{u}) \quad (\text{A.9})$$

Substituting Eq. (A.9) back into Eq. (A.8), we obtain

$$\sum_{n=1}^N \sum_{l=0}^L \sum_{m=-l}^l C_{nlm} j_l\left(\frac{\alpha_{nl} q}{\tau}\right) Y_l^m(\mathbf{u}) \left[-\frac{\alpha_{nl}^2}{\tau^2} g_{nlm}(t) - \frac{d}{dt} g_{nlm}(t) \right] = 0 \quad (\text{A.10})$$

A unique solution exists if and only if $g_{nl}(t) = b_{nl} e^{-\frac{\alpha_{nl}^2 t}{\tau^2}}$ (Chung et al., 2007), and so

$$E(q, \mathbf{u}, t) = \sum_{n=1}^N \sum_{l=0}^L \sum_{m=-l}^l C_{nlm} e^{-\frac{\alpha_{nl}^2 t}{\tau^2}} j_l\left(\frac{\alpha_{nl} q}{\tau}\right) Y_l^m(\mathbf{u}) \quad (\text{A.11})$$

Note that all constants are absorbed into C_{nlm} . In the following sections, we will use the SH basis Y_j proposed in Descoteaux et al. (2011).

Appendix B. Diffusion signal at origin

In diffusion weighted imaging (DWI), $E(0) = 1$. Thus, for our basis, we obtain the following identity:

$$E(0, t = 0) = \sum_n \sum_j C_{nj} j_{l(j)}(0) Y_j(\mathbf{u}) = \frac{1}{\sqrt{4\pi}} \sum_n C_{n1} = 1, \quad (\text{B.1})$$

which holds for any \mathbf{u} within the unit sphere S^2 (i.e. $\mathbf{u} \in S^2$). In deriving Eq. (B.1), we invoked a basic property of the spherical Bessel function that

$$j_l(0) = \begin{cases} 1, & \text{if } l = 0 \\ 0, & \text{if } l \neq 0 \end{cases}$$

and the identity $Y_0^0 = \frac{1}{\sqrt{4\pi}}$.

Appendix C. Derivation of analytical BFOR EAP solution

In the Theory section, we showed that

$$P(p, \mathbf{r}, t) = 4\pi \sum_{n=1}^N \sum_{j=1}^R (-1)^{l(j)/2} C_{nj} e^{-\frac{\alpha_{nl}^2 t}{\tau^2}} Y_j(\mathbf{r}) I_{nl(j)}(p), \quad (\text{C.1})$$

where $I_{nl(j)}(p) = \int_0^\tau q^2 j_{l(j)}\left(\frac{\alpha_{nl} q}{\tau}\right) j_{l(j)}(2\pi q p) dq$. We rewrite $I_{nl(j)}(p)$ in terms of the Bessel function of the first kind:

$$I_{nl(j)}(p) = \frac{1}{2} \sqrt{\frac{\pi\tau}{2\alpha_{nl(j)} p}} \int_0^\tau q J_{l(j)+1/2}\left(\frac{\alpha_{nl} q}{\tau}\right) J_{l(j)+1/2}(2\pi q p) dq \quad (\text{C.2})$$

Recall the Bessel function of first kind $J_k(ax)$, where k is some real-valued constant, satisfies

$$\left(x^2 \frac{d^2}{dx^2} + x \frac{d}{dx} + [a^2 x^2 - k^2] \right) J_k(ax) = 0 \quad (\text{C.3})$$

Thus, by definition of the Bessel function, $J_{l(j)+1/2}\left(\frac{\alpha_{nl} q}{\tau}\right)$ and $J_{l(j)+1/2}(2\pi q p)$ satisfy

$$\left(q \frac{d^2}{dq^2} + \frac{d}{dq} + \left[\frac{\alpha_{nl}^2 q}{\tau^2} - \frac{(l(j)+1/2)^2}{q} \right] \right) J_{l(j)+1/2}\left(\frac{\alpha_{nl} q}{\tau}\right) = 0 \quad (\text{C.4})$$

$$\left(q \frac{d^2}{dq^2} + \frac{d}{dq} + \left[4\pi^2 p^2 q - \frac{(l(j)+1/2)^2}{q} \right] \right) J_{l(j)+1/2}(2\pi q p) = 0, \quad (\text{C.5})$$

respectively. Multiplying Eq. (C.4) by $J_{l(j)+1/2}(2\pi q p)$ and Eq. (C.5)

by $J_{l(j)+1/2}\left(\frac{\alpha_{nl} q}{\tau}\right)$ and then subtracting, we obtain

$$J_{l(j)+1/2}(2\pi q p) \frac{d}{dq} \left[q \frac{d}{dq} J_{l(j)+1/2}\left(\frac{\alpha_{nl} q}{\tau}\right) \right] - J_{l(j)+1/2}\left(\frac{\alpha_{nl} q}{\tau}\right) \frac{d}{dq} \left[q \frac{d}{dq} J_{l(j)+1/2}(2\pi q p) \right] \\ = q \left(4\pi^2 p^2 - \frac{\alpha_{nl}^2}{\tau^2} \right) J_{l(j)+1/2}\left(\frac{\alpha_{nl} q}{\tau}\right) J_{l(j)+1/2}(2\pi q p)$$

Integrating the above from $q = 0$ to $q = \tau$ via integration by parts and noting that $J_{l(j)+1/2}(\alpha_{nl(j)}) = 0$, we have

$$\int_0^\tau q J_{l(j)+1/2}\left(\frac{\alpha_{nl} q}{\tau}\right) J_{l(j)+1/2}(2\pi q p) dq \\ = \frac{\tau J_{l(j)+1/2}(2\pi\tau p) \left[\frac{d}{dq} J_{l(j)+1/2}\left(\frac{\alpha_{nl} q}{\tau}\right) \right]_{q=\tau}}{4\pi^2 p^2 - \frac{\alpha_{nl}^2}{\tau^2}} \quad (\text{C.6})$$

The right side of Eq. (C.6) can be simplified via the Bessel recurrence relations $\frac{d}{dx} J_k(x) = \frac{1}{2}(J_{k-1}(x) - J_{k+1}(x))$:

$$\int_0^\tau q J_{l(j)+1/2}\left(\frac{\alpha_{nl} q}{\tau}\right) J_{l(j)+1/2}(2\pi q p) dq \\ = \frac{\alpha_{nl(j)} J_{l(j)+1/2}(2\pi\tau p)}{2(4\pi^2 p^2 - \frac{\alpha_{nl}^2}{\tau^2})} \left(J_{l(j)-1/2}(\alpha_{nl(j)}) - J_{l(j)+3/2}(\alpha_{nl(j)}) \right) \quad (\text{C.7})$$

Using the Bessel recurrence relation $J_{k+1}(x) = \frac{2k}{x} J_k(x) - J_{k-1}(x)$, we obtain $J_{l(j)+3/2}(\alpha_{nl(j)}) = -J_{l(j)-1/2}(\alpha_{nl(j)})$, and so we can rewrite Eq. (C.7) as

$$\int_0^\tau q J_{l(j)+1/2}\left(\frac{\alpha_{nl} q}{\tau}\right) J_{l(j)+1/2}(2\pi q p) dq \\ = \frac{\alpha_{nl(j)} J_{l(j)-1/2}(\alpha_{nl(j)}) J_{l(j)+1/2}(2\pi\tau p)}{4\pi^2 p^2 - \frac{\alpha_{nl}^2}{\tau^2}}, \quad (\text{C.8})$$

Thus, substituting Eq. (C.8) back into Eq. (C.2), we obtain

$$I_{nl(j)}(p) = \frac{1}{2} \sqrt{\frac{\pi\tau}{2p}} \frac{\sqrt{\alpha_{nl(j)}} J_{l(j)-1/2}(\alpha_{nl(j)}) J_{l(j)+1/2}(2\pi\tau p)}{\left(4\pi^2 p^2 - \frac{\alpha_{nl}^2}{\tau^2} \right)},$$

and so the diffusion propagator is then

$$P(p, \mathbf{r}, t) = 2\tau \sqrt{2\pi^3} \sum_{n=1}^N \sum_{j=1}^R (-1)^{l(j)/2} C_{nj} e^{-\frac{\alpha_{nl}^2 t}{\tau^2}} Y_j(\mathbf{r}) \frac{\sqrt{\alpha_{nl(j)}} J_{l(j)-1/2}(\alpha_{nl(j)}) j_{l(j)}(2\pi\tau p)}{\left(4\pi^2 p^2 - \frac{\alpha_{nl}^2}{\tau^2} \right)} \quad (\text{C.9})$$

Appendix D. Derivation of BFOR zero-displacement probability

We can derive P_0 by evaluating Eq. (C.9) at $p=0$:

$$P_0 = P(p=0, \mathbf{r}) = 2\tau\sqrt{2\pi^3} \sum_{n=1}^N C_{n1} Y_1(\mathbf{r}) \frac{\sqrt{\alpha_{n0}} J_{-1/2}(\alpha_{n0})}{-\frac{\alpha_{n0}^2}{\tau}} \\ = \frac{2\tau\sqrt{2\pi^3}}{\sqrt{4\pi}} \sum_{n=1}^N C_{n1} \frac{\sqrt{\alpha_{n0}} \sqrt{\frac{2}{\pi\alpha_{n0}} \cos(\alpha_{n0})}}{-\frac{\alpha_{n0}^2}{\tau}} = 2\sqrt{\pi}\tau^3 \sum_{n=1}^N C_{n1} \frac{(-1)^{n+1}}{\alpha_{n0}^2}, \quad (\text{D.1})$$

where we used the relation $J_{-1/2}(x) = \sqrt{\frac{2}{\pi x}} \cos(x)$.

Appendix E. Relationship between MSD and diffusion signal in q -space

We define the wave vector \mathbf{q} as $\mathbf{q} = q_x \hat{i} + q_y \hat{j} + q_z \hat{k}$ and the radius vector in propagator space \mathbf{p} as $\mathbf{p} = p_x \hat{i} + p_y \hat{j} + p_z \hat{k}$. The norm of \mathbf{p} is $p = \sqrt{p_x^2 + p_y^2 + p_z^2}$.

Since the diffusion signal and EAP are FT pairs, then the inversion of Eq. (1) gives

$$E(\mathbf{q}) = \int P(\mathbf{p}) e^{2\pi i \mathbf{q} \cdot \mathbf{p}} d^3 \mathbf{p} = \int P(\mathbf{p}) e^{2\pi i (q_x p_x + q_y p_y + q_z p_z)} d^3 \mathbf{p} \quad (\text{E.1})$$

Taking the second derivative of $E(\mathbf{q})$ with respect to q_x , q_y , and q_z gives

$$\frac{\partial^2 E(\mathbf{q})}{\partial q_x^2} = (2\pi i)^2 \int p_x^2 P(\mathbf{p}) e^{2\pi i \mathbf{q} \cdot \mathbf{p}} d^3 \mathbf{p} \\ \frac{\partial^2 E(\mathbf{q})}{\partial q_y^2} = (2\pi i)^2 \int p_y^2 P(\mathbf{p}) e^{2\pi i \mathbf{q} \cdot \mathbf{p}} d^3 \mathbf{p} \\ \frac{\partial^2 E(\mathbf{q})}{\partial q_z^2} = (2\pi i)^2 \int p_z^2 P(\mathbf{p}) e^{2\pi i \mathbf{q} \cdot \mathbf{p}} d^3 \mathbf{p}$$

The sum of the derivatives is simply the Laplacian operator acting on $E(\mathbf{q})$:

$$\nabla^2 E(\mathbf{q}) = \frac{\partial^2 E(\mathbf{q})}{\partial q_x^2} + \frac{\partial^2 E(\mathbf{q})}{\partial q_y^2} + \frac{\partial^2 E(\mathbf{q})}{\partial q_z^2} = (2\pi i)^2 \int p^2 P(\mathbf{p}) e^{2\pi i \mathbf{q} \cdot \mathbf{p}} d^3 \mathbf{p} \quad (\text{E.2})$$

Note that the Laplacian of $E(\mathbf{q})$ evaluated at $\mathbf{q}=0$ is related to the second moment of the EAP. Thus, the MSD is

$$\langle p^2 \rangle = \frac{-1}{4\pi^2} \nabla^2 E(\mathbf{q}) \Big|_{\mathbf{q}=0} \quad (\text{E.3})$$

For the case of DTI, where $E(q, \mathbf{u}) = e^{-4\pi^2 q^2 (\Delta - \delta/3) \mathbf{u}^T \mathbf{D} \mathbf{u}}$, Eq. (E.3) simplifies to the Einstein relation

$$\langle p^2 \rangle = 6(\Delta - \delta/3) MD \quad (\text{E.4})$$

E.1. Derivation of BFOR MSD

The BFOR signal basis is an eigenfunction of the Laplacian operator, with eigenvalues $-\frac{\alpha_{nl(j)}^2}{\tau^2}$. Hence

$$\nabla^2 E(\mathbf{q}) = - \sum_{n=1}^N \sum_{j=1}^R C_{nj} \left(\frac{\alpha_{nl(j)}}{\tau} \right)^2 e^{-\alpha_{nl(j)}^2 t / \tau^2} j_{l(j)} \left(\frac{\alpha_{nl(j)} q}{\tau} \right) Y_j(\mathbf{u}) \quad (\text{E.5})$$

Evaluating the Laplacian of $E(\mathbf{q})$ at $q=0$ gives

$$\nabla^2 E(\mathbf{q}) \Big|_{\mathbf{q}=0} = \frac{-1}{2\sqrt{\pi}\tau^2} \sum_{n=1}^N C_{n1} \alpha_{n0}^2 e^{-\alpha_{n0}^2 t / \tau^2} \quad (\text{E.6})$$

Substituting Eq. (E.6) into Eq. (E.3), we obtain

$$\langle p^2 \rangle_{\text{BFOR}} = \frac{1}{8\pi^2 \tau^2} \sum_{n=1}^N C_{n1} \alpha_{n0}^2, \quad (\text{E.7})$$

where we dropped the smoothing term.

Appendix F. Relationship between QIV and EAP in q -space

Using the definition of QIV, we have

$$QIV^{-1} = \int q^2 E(\mathbf{q}) d^3 \mathbf{q} = \int q^2 \left[\int P(\mathbf{p}) e^{2\pi i \mathbf{q} \cdot \mathbf{p}} d^3 \mathbf{p} \right] d^3 \mathbf{q} \\ = \int P(\mathbf{p}) t \left[\int q^2 e^{2\pi i \mathbf{q} \cdot \mathbf{p}} d^3 \mathbf{q} \right] d^3 \mathbf{p} \quad (\text{F.1})$$

The Dirac delta function is defined as

$$\delta(\mathbf{p}) = \int e^{2\pi i \mathbf{q} \cdot \mathbf{p}} d^3 \mathbf{q} \quad (\text{F.2})$$

Taking the second derivative of $\delta(\mathbf{p})$ with respect to p_x , p_y , and p_z gives

$$\frac{\partial^2 \delta(\mathbf{p})}{\partial p_x^2} = (2\pi i)^2 \int q_x^2 e^{2\pi i \mathbf{q} \cdot \mathbf{p}} d^3 \mathbf{q} \\ \frac{\partial^2 \delta(\mathbf{p})}{\partial p_y^2} = (2\pi i)^2 \int q_y^2 e^{2\pi i \mathbf{q} \cdot \mathbf{p}} d^3 \mathbf{q} \\ \frac{\partial^2 \delta(\mathbf{p})}{\partial p_z^2} = (2\pi i)^2 \int q_z^2 e^{2\pi i \mathbf{q} \cdot \mathbf{p}} d^3 \mathbf{q}$$

The sum of the derivatives is simply the Laplacian operator acting on $\delta(\mathbf{p})$:

$$\nabla^2 \delta(\mathbf{p}) = \frac{\partial^2 \delta(\mathbf{p})}{\partial p_x^2} + \frac{\partial^2 \delta(\mathbf{p})}{\partial p_y^2} + \frac{\partial^2 \delta(\mathbf{p})}{\partial p_z^2} = (2\pi i)^2 \int q^2 e^{2\pi i \mathbf{q} \cdot \mathbf{p}} d^3 \mathbf{q} \quad (\text{F.3})$$

Thus, Eq. (F.1) becomes

$$QIV^{-1} = \frac{-1}{4\pi^2} \int P(\mathbf{p}) \left[\nabla^2 \delta(\mathbf{p}) \right] d^3 \mathbf{p} \quad (\text{F.4})$$

Since the Laplacian operator ∇^2 is Hermitian and the EAP and $\delta(\mathbf{p})$ are real-valued, Eq. (F.4) can be equivalently stated as

$$QIV^{-1} = \frac{-1}{4\pi^2} \int P(\mathbf{p}) \left[\nabla^2 \delta(\mathbf{p}) \right] d^3 \mathbf{p} = \frac{-1}{4\pi^2} \int \delta(\mathbf{p}) \left[\nabla^2 P(\mathbf{p}) \right] d^3 \mathbf{p}$$

Exploiting the property of the Dirac delta function that $\int_{-\infty}^{\infty} f(x) \delta(x) dx = f(0)$, we have

$$QIV^{-1} = \frac{-\nabla^2 P(\mathbf{p}) \Big|_{\mathbf{p}=0}}{4\pi^2}, \quad (\text{F.5})$$

which is very similar in form to Eq. (E.3). Thus, whereas the MSD directly varies with the Laplacian of the diffusion signal evaluated at the origin, the QIV inversely varies with the Laplacian of the EAP evaluated at the origin.

F.1. Derivation of BFOR QIV

$$\begin{aligned} QIV^{-1} &= \int q^2 E(\mathbf{q}) d^3 \mathbf{q} \approx \sum_n \sum_j C_{nj} \int Y_j(\mathbf{u}) d^2 \mathbf{u} \int_0^\tau q^4 j_{l(j)} \left(\frac{\alpha_{nl(j)} q}{\tau} \right) dq \\ &= \sqrt{4\pi} \sum_n C_{n1} \int_0^\tau q^4 j_0 \left(\frac{\alpha_{n0} q}{\tau} \right) dq = \sqrt{4\pi} \tau \sum_n \frac{C_{n1}}{\alpha_{n0}} \int_0^\tau q^3 \sin \left(\frac{\alpha_{n0} q}{\tau} \right) dq \end{aligned}$$

The last integral can easily be solved via integration by parts, and so the QIV is

$$QIV_{BFOR} = \frac{1}{2\sqrt{\pi}\tau^5 \sum_{n=1}^N (-1)^n C_{n1} \frac{(6-\alpha_{n0}^2)}{\alpha_{n0}^3}} \quad (F.6)$$

References

- Aganj, I., Lenglet, C., Sapiro, G., Yacoub, E., Ugurbil, K., Harel, N., 2010. Reconstruction of the orientation distribution function in single- and multiple-shell q-ball imaging within constant solid angle. *Magn. Reson. Med.* 64, 554–566.
- Alexander, A.L., Hasan, K.M., Lazar, M., Tsuruda, J.S., Parker, D.L., 2001. Analysis of partial volume effects in diffusion-tensor MRI. *Magn. Reson. Med.* 45, 770–780.
- Assaf, Y., Cohen, Y., 1998. Non-mono-exponential attenuation of water and n-acetyl aspartate signals due to diffusion in brain tissue. *J. Magn. Reson.* 131, 69–85.
- Assaf, Y., Cohen, Y., 2000. Assignment of the water slow-diffusing compartment in the central nervous system using q-space diffusion MRS: implications for fiber tract imaging. *Magn. Reson. Med.* 43, 191–199.
- Assaf, Y., Mayk, A., Cohen, Y., 2000. Displacement imaging of spinal cord using q-space diffusion-weighted MRI. *Magn. Reson. Med.* 44, 713–722.
- Assaf, Y., Ben Bashat, D., Chapman, J., Peled, S., Biton, I.E., Kafri, M., Segev, Y., Hendler, T., Korczyn, A.D., Graif, M., Cohen, Y., 2002. High b-value q-space analyzed diffusion-weighted MRI: application to multiple sclerosis. *Magn. Reson. Med.* 47, 115–126.
- Assemlal, H.E., Tschumperlé, D., Brun, L., 2009a. Efficient and robust computation of PDF features from diffusion MR signal. *Med. Image Anal.* 13, 715–729.
- Assemlal, H.E., Tschumperlé, D., Brun, L., 2009b. Evaluation of q-space sampling strategies for the diffusion magnetic resonance imaging. *MICCAI*, pp. 482–489.
- Assemlal, H.E., Campbell, J., Pike, B., Siddiqi, K., 2011. Apparent intravoxel fibre population dispersion (FPD) using spherical harmonics. *MICCAI*, pp. 157–165.
- Bar-Shir, A., Avram, L., Ozarslan, E., Basser, P.J., Cohen, Y., 2008. The effect of the diffusion time and pulse gradient duration ratio on the diffraction pattern and the structural information estimated from q-space diffusion MR. *J. Magn. Reson.* 194, 230–236.
- Bar-Shir, A., Ducan, I.D., Cohen, Y., 2009. QSI and DTI of excised brain of the myelin-deficient rat. *Neuroimage* 48, 109–116.
- Basser, P.J., 2002. Relationships between diffusion tensor and q-space MRI. *Magn. Reson. Med.* 47, 392–397.
- Basser, P.J., Pierpaoli, C., 1996. Microstructural and physiological features of tissues elucidated by quantitative-diffusion-tensor MRI. *J. Magn. Reson.* 111, 209–219.
- Basser, P.J., Mattiello, J., LeBihan, D., 1994. MR diffusion tensor spectroscopy and imaging. *Biophys. J.* 66, 259–267.
- Callaghan, P.T., 1991. *Principles of Nuclear Magnetic Resonance Microscopy*. Oxford University Press, Oxford.
- Canales-Rodriguez, E.J., Melie-Garcia, L., Iturria-Medina, Y., 2009. Mathematical description of q-space in spherical coordinates: exact q-ball imaging. *Magn. Reson. Med.* 61, 1350–1367.
- Canales-Rodriguez, E.J., Iturria-Medina, Y., Aleman-Gomez, Y., Melie-Garcia, L., 2010. Deconvolution in diffusion spectrum imaging. *Neuroimage* 50, 136–149.
- Caruyer, E., Deriche, R., 2012. Optimal regularization for MR diffusion signal. *IEEE International Symposium on Biomedical Imaging*.
- Caruyer, E., Cheng, J., Lenglet, C., Sapiro, G., Jiang, T., Deriche, R., 2011. Optimal design of multiple q-shells experiments for diffusion MRI. *MICCAI Workshop on Computational Diffusion MRI-CDMRI'11*.
- Cheng, J., Ghosh, A., Deriche, R., Jiang, T., 2010a. Model-free, regularized, fast, and robust analytical orientation distribution function estimation. *MICCAI*, pp. 648–656.
- Cheng, J., Ghosh, A., Jiang, T., Deriche, R., 2010b. Model-free and analytical EAP reconstruction via spherical polar Fourier diffusion MRI. *MICCAI*, pp. 590–597.
- Chung, M.K., Dalton, K.M., Shen, L., Evans, A.C., Davidson, R.J., 2007. Weighted Fourier series representation and its application to quantifying the amount of gray matter. *IEEE Trans. Med. Imaging* 26, 566–581.
- Clark, C.A., Le Bihan, D., 2000. Water diffusion compartmentation and anisotropy at high b values in the human brain. *Magn. Reson. Med.* 44, 852–859.
- Cohen, Y., Assaf, Y., 2002. High b-value q-space analyzed diffusion-weighted MRS and MRI in neuronal tissues: a technical review. *NMR Biomed.* 15, 516–542.
- Cook, P.A., Bai, Y., Nedjati-Gilani, S., Seunarine, K.K., Hall, M.G., Parker, G.J., Alexander, D.C., 2006. Camino: open-source diffusion-MRI reconstruction and processing. *Proc. Intl. Soc. Mag. Reson. Med.*
- Descoteaux, M., Angelino, E., Fitzgibbons, S., Deriche, R., 2007. Regularized, fast, and robust analytical q-ball imaging. *Magn. Reson. Med.* 58, 497–510.
- Descoteaux, M., Deriche, R., LeBihan, D., Mangin, J.F., Poupon, C., 2011. Multiple q-shell diffusion propagator imaging. *Med. Image Anal.* 15, 603–621.
- Du, J., Goh, A., Qiu, A., 2012. Diffeomorphic metric mapping of high angular resolution diffusion imaging based on riemannian structure of orientation distribution functions. *IEEE Trans. Med. Imaging* 31, 1021–1033.
- Frank, L.R., 2001. Anisotropy in high angular resolution diffusion-weighted MRI. *Magn. Reson. Med.* 45, 935–939.
- Ghosh, A., Deriche, R., 2010. Fast and closed-form ensemble-average-propagator approximation from the 4th-order diffusion tensor. *IEEE International Symposium on Biomedical Imaging*.
- Hess, C.P., Mukherjee, P., Han, E.T., Xu, D., Vigneron, D.B., 2006. Q-ball reconstruction of multimodal fiber orientations using the spherical harmonic basis. *Magn. Reson. Med.* 56, 104–117.
- Hosseinbor, A.P., Chung, M.K., Wu, Y.C., Alexander, A.L., 2011. Bessel Fourier orientation reconstruction: an analytical EAP reconstruction using multiple shell acquisitions in diffusion MRI. *MICCAI*, pp. 217–225.
- Katkovnik, V., 1999. A new method for varying adaptive bandwidth selection. *IEEE Trans. Signal Process.* 47, 2567–2571.
- Maier, S.E., Vajapeyam, S., Mamata, H., Westin, C.F., Jolesz, F.A., Mulkern, R.V., 2004. Biexponential diffusion tensor analysis of human brain diffusion data. *Magn. Reson. Med.* 51, 321–330.
- Mair, R.W., Sen, P.N., Hurlimann, M.D., Patz, S., Cory, D.G., Walsworth, R.L., 2002. The narrow pulse approximation and long length scale determination in xenon gas diffusion NMR studies of model porous media. *J. Magn. Reson.* 156, 202–212.
- Merlet, S., Caruyer, E., Deriche, R., 2011. Impact of radial and angular sampling on multiple shells acquisition in diffusion MRI. *MICCAI*, pp. 113–121.
- Mulkern, R.V., Gudbjartsson, H., Westin, C.F., Zengingonul, H.P., Gartner, W., R., G.C., Robertson, R., W., K., Schwartz, R., Holtzman, D., Jolesz, F.A., Maier, S.E., 1999. Multi-component apparent diffusion coefficients in human brain. *NMR Biomed.* 12, 51–62.
- Niendorf, T., Dijkhuizen, R.M., Norris, D.G., van Lookeren Campagne, M., Nicolay, K., 1996. Biexponential diffusion attenuation in various states of brain tissue: implications for diffusion-weighted imaging. *Magn. Reson. Med.* 36, 847–857.
- Ozarslan, E., Shepherd, T.M., Vemuri, B.C., Blackband, S.J., Mareci, T.H., 2006. Resolution of complex tissue microarchitecture using the diffusion orientation transform (DOT). *Neuroimage* 31, 1086–1103.
- Ozarslan, E., Koay, C.G., Basser, P.J., 2008. Simple harmonic oscillator based estimation and reconstruction for one-dimensional q-space MR. *Proc. Intl. Soc. Mag. Reson. Med.*
- Ozarslan, E., Koay, C., Shepherd, T.M., Blackband, S.J., Basser, P.J., 2009. Simple harmonic oscillator based reconstruction and estimation for three-dimensional q-space MRI. *Proc. Intl. Soc. Mag. Reson. Med.*
- Rathi, Y., Michailovic, O., Setsompop, K., Bouix, S., Shenton, M.E., Westin, C.F., 2011. Sparse multi-shell diffusion imaging. *MICCAI*, pp. 58–65.
- Stejskal, E., Tanner, J., 1965. Spin diffusion measurements: spin echoes in the presence of a time-dependent field gradient. *J. Chem. Phys.* 42, 288–292.
- Tournier, J.D., Calamante, F., Gadian, D.G., Connelly, A., 2004. Direct estimation of the fiber orientation density function from diffusion-weighted MRI data using spherical deconvolution. *Neuroimage* 23, 1176–1185.
- Tuch, D.S., 2004. Q-ball imaging. *Magn. Reson. Med.* 52, 1358–1372.
- Tuch, D.S., Reese, T.G., Wiegell, M.R., Makris, N., Belliveau, J.W., Weeden, V.J., 2002. High angular resolution diffusion imaging reveals intravoxel white matter fiber heterogeneity. *Magn. Reson. Med.* 48, 577–582.
- Weeden, V.J., Hagmann, P., Tseng, W.Y.I., Reese, T.G., Weisskoff, R.M., 2005. Mapping complex tissue architecture with diffusion spectrum magnetic resonance imaging. *Magn. Reson. Med.* 54, 1377–1386.
- Wiegell, M.R., Larsson, H.B., Wedeen, V.J., 2000. Fiber crossing in human brain depicted with diffusion tensor MR imaging. *Radiology* 217, 897–903.
- Wong, S.T.S., Roos, M.S., 1994. A strategy for sampling on a sphere applied to 3D selective RF pulse design. *Magn. Reson. Med.* 32, 778–784.
- Wu, Y.C., Alexander, A.L., 2007. Hybrid diffusion imaging. *Neuroimage* 36, 617–629.
- Wu, Y.C., Field, A.S., Alexander, A.L., 2008. Computation of diffusion function measures in q-space using magnetic resonance hybrid diffusion imaging. *IEEE Trans. Med. Imaging* 27, 858–865.
- Wu, Y.C., Field, A.S., Duncan, I.D., Samsonov, A.A., Kondo, Y., Tudorascu, D., Alexander, A.L., 2011. High b-value and diffusion tensor imaging in a canine model of dysmyelination and brain maturation. *Neuroimage* 58, 829–837.
- Yeh, C.H., Cho, K.H., Lin, H.C., Wang, J.J., Lin, C.P., 2008. Reduced encoding diffusion spectrum imaging implemented with a bi-Gaussian model. *IEEE Trans. Med. Imaging* 27, 1415–1424.